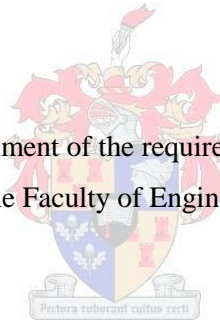


Liquid extraction from air-cooled condenser steam ducts

Japie van der Westhuizen

Thesis presented in partial fulfilment of the requirements for the degree of Master of Engineering (Mechanical) in the Faculty of Engineering at Stellenbosch University



Supervisor: Dr J Hoffmann

December 2015

DECLARATION

By submitting this thesis electronically, I declare that the entirety of the work contained therein is my own, original work, that I am the sole author thereof (save to the extent explicitly otherwise stated), that reproduction and publication thereof by Stellenbosch University will not infringe any third party rights and that I have not previously in its entirety or in part submitted it for obtaining any qualification.

Signature:

Date:

ABSTRACT

Matimba Power Station in South Africa experiences erosion of its air-cooled condenser (ACC) bundle tubes, as stated in an ACC degradation report by Eskom. This erosion is caused by water droplets (wet steam) travelling at high velocities. Impurities due to demineralization system failures and corroded metal are carried via these water droplets to the ACC bundles. The impurities lower the pH level of the water droplets, promoting corrosion. If the impurities that are carried to the ACC bundles could be reduced through water/steam separation, the erosion of the ACC bundles would be reduced. An aerodynamic water/steam separator is designed to reduce the pressure loss caused by the separator and the best location for liquid extraction is identified in the ducting. To design such a separator certain sensitivities need to be evaluated like the shape of the separator and also the sensitivities on the shape itself. To find the best location for the separator in terms of the amount of liquid that can be extracted, it should be known where most of the droplets flow in the flow domain. There is no information regarding the droplet size distribution and certain assumptions need to be made. Different models are used for different droplet sizes and these models are also investigated in this study and identified for the conditions on the power station. The shape and location for the separator is identified with an airfoil shape placed on one of the vanes in the bend of the ducting.

OPSOMMING

Matimba Kragstasie in Suid-Afrika maak melding van erosie op die stasie se lugverkoelde kondensatorbuis in 'n Eskom-verslag oor die degradasie van lugverkoelde kondensatorbuis. Hierdie erosie word veroorsaak deur waterdruppels (nat stoom) wat teen groot snelhede beweeg. Onsuiverhede afkomstig van gedemineraliseerde sisteem probleme en verroesde metaal word in die druppels na die kondensatorbuis vervoer. Die onsuiverhede in die waterdruppels verlaag die waterdruppels se pH, wat op sy beurt korrosie veroorsaak. Indien die druppels wat die onsuiverhede bevat met behulp van water-/stoomskeiding onttrek kan word voordat hulle die kondensatorbuis bereik, kan die erosie op die kondensator verminder word. 'n Aerodinamiese water/stoom skeier is ontwerp om die kleinste drukval wat deur die skeier veroorsaak word, te verminder, asook die beste plasing vir die skeier in die vloeikanaal. Om so 'n skeier te ontwerp moet sekere sensitiviteite getoets word soos die vorm van die skeier asook die sensitiviteite op die vorm self. Om die beste plasing vir die skeier te kry in terme van die plek waar die meeste vloeistof onttrek kan word, moet die plek bekend wees waar die meeste van die druppels vloei in die vloeikanaal. Daar is geen informasie aangaande die druppel grootte en verspreiding op die kragstasie nie en dus moet sekere aannames gemaak word. Verskillende modelle word gebruik vir verskillende druppel groottes en hierdie modelle word ondersoek en bepaal in hierdie studie vir die kondisies op die kragstasie. Die vorm en plasing van die skeier is bepaal met 'n vlerkprofiel vorm op een van die gids wieke in die draai van die vloeikanaal.

DEDICATION

This thesis is dedicated to Japie and Jalien van der Westhuizen, parents of Japie van der Westhuizen (author), for their constant support, motivation and advice throughout the project.

ACKNOWLEDGEMENTS

Firstly, the author wants to thank Dr Jaap Hoffman for excellent guidance, patience and support whilst supervising the project and also for playing a big role in the success of the project.

Thanks to Johannes Pretorius and Francois du Preez for mentoring the project from Eskom and providing guidance, comments and support to enable the author to complete the project successfully.

Thanks to Louis Jestin, Malcolm Fawkes and Nicolaas Basson for providing the study opportunity by promoting the EPPEI (Eskom Power Plant Engineering Institute) programme from where the project originated.

Thanks to Anton Hart for financial support, permission and motivation with regard to the completion of the study.

Lastly, special thanks to Eskom for promoting the EPPEI programme to give engineers the opportunity to undertake postgraduate studies.

CONTENTS

	Page
Abstract.....	i
Opsomming.....	ii
Dedication.....	iii
Acknowledgements.....	iv
Contents.....	iv
List of tables.....	vii
List of figures.....	viii
List of abbreviations.....	x
Chapter 1.....	1
INTRODUCTION.....	1
Chapter 2.....	6
RATIONALE.....	6
2.1 Test setup.....	7
2.2 Test results.....	9
2.3 Discussion and conclusion of the test setup.....	10
Chapter 3.....	11
LITERATURE STUDY.....	11
3.1 Turbulence model.....	11
3.1.1 Spalart-Allmaras model.....	13
3.1.2 k- ϵ Models.....	13
3.1.3 k- ω Models.....	13
3.2 Euler-Lagrange and Euler-Euler approaches.....	16
3.3 Discrete phase modelling.....	16
3.4 Drag laws.....	18
3.5 Stokes number.....	21
3.6 Lift forces.....	23
3.7 Wall film model theory.....	26
3.8 Shape effects on drag.....	28
Chapter 4.....	30
COMPUTATIONAL FLUID DYNAMICS MODEL.....	30
4.1 Validation of the model.....	30
4.2 Geometry, mesh and grid independence.....	33
4.2.1 Geometry.....	33
4.2.2 Mesh.....	34
4.2.3 Boundary conditions.....	38
4.2.4 Grid independence.....	39
4.3 Droplet size range.....	42
4.3.1 Computational domain.....	43
4.3.2 Results and discussion.....	44
4.4 Submodels.....	46
4.4.1 Drag law.....	46
4.4.2 External forces.....	47

4.4.3 Wall film model.....	48
4.5 Separator design	49
4.5.1 Shapes	49
4.5.2 Airfoil optimization	55
4.5.4 Placement of the separator on the vane	58
Chapter 5.....	64
CONCLUSION	64
Chapter 6.....	67
RECOMMENDATIONS	67
REFERENCES	68
Appendix A.....	70
DRAWINGS	70
A.1: Duct	70
A.2: Guide vanes	71
Appendix B.....	72
B.1 Velocity of 100 µm droplets falling under the force of gravity	72

LIST OF TABLES

	Page
Table 2.1: Laboratory results Unit 6 ACCCT/ACC duct – samples 17 and 18 Jan 2011	7
Table 2.2: Results of liquid extracted during preliminary testing	10
Table 3.1: RANS turbulence model comparison	15
Table 4.1: Grid independency for the Terminal velocity of a 100 μm droplet	31
Table 4.2: Step length factor independency	32
Table 4.3: Properties of fluids	36
Table 4.4: Relaxation factors	37
Table 4.5: Inlet and outlet boundary conditions	39
Table 4.6: Pressure drop for different cell sizes	41
Table 4.7: Evaluation of discretisation schemes	42
Table 4.8: Properties of fluids and boundary conditions	43
Table 4.9: The maximum droplet size for the size range	44
Table 4.10: The 500 micron droplet's flow behaviour when the inlet velocity is varied	44
Table 4.11: The minimum droplet size for the size range	45
Table 4.12: Effect of the SDL and DDL on the accretion rate on the vanes and droplet breakup	47
Table 4.13: Accretion rate of different size droplets on the vanes	48
Table 4.14: Behaviour of droplets for different size film heights	49
Table 4.15: Grid independence for the two dimensional flow domain	51
Table 4.16: Pressure loss for five different shapes	52
Table 4.17: Pressure loss for different radius ratios for the elliptical section of the airfoil	56
Table 4.18: Effect of length of the tail extension in terms of pressure loss	57
Table 4.19: The accretion rate of the droplets in $\text{kg}/\text{m}^2\text{-s}$ that collides with the turning vanes	60
Table 4.20: Area of each vane	60
Table 4.21: Mass flow rate of different sizes of droplets colliding with the turning vanes	61
Table 4.22: Effect of pressure when the separator is moved on the vane	63

LIST OF FIGURES

	Page
Figure 1.1: Corrosion on entrance to the ACC tubes.....	3
Figure 2.1: Aerial view of Matimba Power Station.....	6
Figure 2.2: Side view of the ACC ducts.	8
Figure 2.3: Here (a), left, shows the location and length of the separator at the downstream side of the bend, surrounded in Figure 2.2, while (b) is a detailed sketch of the separator welded onto the trailing edge of the vane viewed from the side.	9
Figure 3.1: Ohnesorge number for different sizes of droplets	20
Figure 3.2: Weber numbers for droplets ranging from 50-500 micron	21
Figure 3.3: Stokes numbers for droplet sizes ranging from 50 to 500 μm	23
Figure 3.4: Gravitational-, Saffman- and Magnus forces on droplets that are ranging from 50-500 μm	25
Figure 3.5: Dimensionless impact energy for different liquid film heights for droplet sizes between 1 and 500 μm with a relative velocity of 76 m/s	28
Figure 3.6: Drag on different objects with aerodynamic shapes	29
Figure 4.1: Velocity of 100 micron droplets falling under the force of gravity	32
Figure 4.2: Average velocity of 100 micron droplets falling under the force of gravity.....	33
Figure 4.3: Layout and dimensions of the duct	34
Figure 4.4: Meshed first half of the duct with tetrahedral cells used for grid dependency	36
Figure 4.5: Here (a) shows the wall boundary of the outside edges of the flow domain, and (b) illustrates the vanes and bypass wall boundary condition	38
Figure 4.6: Inlet (a) and outlet (b) boundary conditions.....	39
Figure 4.7: Symmetry boundary condition	40
Figure 4.8: Here (a) and (b) are the inlet and outlet boundary conditions respectively, (c) represents the wall boundary condition at the bypass, (d) is the symmetrical boundary condition and (e) is the duct wall boundary condition	43
Figure 4.9: Velocity vectors passing the downstream end of vane five	50
Figure 4.10: Airfoil geometry.....	51
Figure 4.11: Velocity profile for the airfoil.....	52
Figure 4.12: Velocity profile for the sphere.....	53
Figure 4.13: Velocity profile for the bullet.....	53
Figure 4.14: Velocity profile for the prism.....	54
Figure 4.15: Velocity profile for the flat plate.....	54
Figure 4.16: Velocity profile for the ellipse with a radius ratio of 14.....	56
Figure 4.17: Tail extension of the airfoil with length 90 mm.....	57

Figure 4.18: Velocity profile of the most aerodynamic airfoil58
Figure 4.19: Here (a) is the velocity profile at the symmetric boundary of the duct
and (b) is the pressure profile at the cross section illustrated in (a)...59
Figure 4.20: Separator placement on the vane.....62

LIST OF ABBREVIATIONS

ACC	air-cooled condenser
ACCCT	air-cooled condenser condensate tank
CFD	computational fluid dynamics
DDL	dynamic drag law
LES	large-eddy simulation
LPT	low-pressure turbine
RANS	Reynolds-Averaged Navier-Stokes
RNG	renormalisation group
RSM	Reynolds stress models
SDL	spherical drag law
SSD	stochastic secondary droplet
SST	shear-stress transport

NOMENCLATURE

A	area of the duct	(m ²)
C	coefficient	
CI	confidence interval	
D	duct inner diameter	(m)
d	cross-section of droplet	(m)
E	impact energy	
F	force	(N)
f	friction factor	
h	height	(m)
\dot{m}	mass flow	(kg/s)
On	Ohnesorge number	
\dot{R}	accretion rate	(kg/m ² -s)
r	radius of droplet	(m)
Re	Reynolds number	
Stk	Stokes number	
t	time	(s)
u	velocity	(m/s)
We	Weber number	

y	distance in y-direction	(m)
V	volume	(m ³)
x	distance in x-direction	(m)
α	volume fraction	
δ	thickness	(m)
μ	dynamic viscosity	(kg/m ² s)
ρ	density	(kg/m ³)
σ	surface tension	(N/m)
τ	response time	(s)
ω	specific dissipation rate	(m ² /s ³)

Subscripts

bl	boundary layer
c	critical
D	drag
DW	Darcy-Weisbach
d	droplet
f	fluid
G	gravitational
L	lift

<i>l</i>	liquid
<i>M</i>	Magnus
<i>m</i>	mixture
<i>p</i>	particle
<i>r</i>	relative
<i>S</i>	Saffman
<i>s</i>	characteristic or system
<i>t</i>	terminal
<i>v</i>	vapour

CHAPTER 1

INTRODUCTION

Due to the limited water supply in South Africa, some power stations were built with a dry cooling system, using air as coolant. One of these dry cooling systems is in the form of an air-cooled condenser (ACC) and has advantages over other cooling systems. The availability of water is the main deciding factor when an ACC is built instead of a water cooled system, like for Matimba Power Station which is the focus of this investigation.

Matimba Power Station, a coal-fired power plant operated by Eskom, is close to Lephalale in Limpopo Province. It was commissioned between 1988 and 1993 and has been running continuously since then. This station has a capacity of 3 990 megawatt, provided by six 665 megawatt units, and has a minimum lifespan of 35 years. Matimba is the largest direct dry cooling system in the world and is the holder of the world record of 80 days for six units on load. Matimba and Majuba are currently the only working power stations using this cooling system to cool wet steam in Eskom's fleet (Eskom, 2013).

In the steam cycle in a power station using ACCs, there is a continual loss of cycle water. The majority of this loss is due to blowdowns for pressure relief and chemistry control and minor losses like tube and valve leaks. Therefore, a continual source of incoming water (make-up water) is needed. This water is demineralised and treated to remove dissolved impurities and to feed water to the boiler with a high pH (alkaline), high purity and low oxygen level to prevent corrosion. Impurities cause build-up in the steam cycle. Superheated steam is generated in the boiler and is saturated as it flows to the low-pressure turbine (LPT). As wet steam passes the stages in the LPT, the steam becomes condensed as the steam region expands in the turbine and droplets are formed. The input used for the steam duct in this study is assumed to be the outlet condition of the LPT steam. These droplets can cause damage to ACCs.

This study originates through degradation of the ACCs at Matimba Power Station, caused by high-speed water droplets in the steam cycle. These droplets arise from expansion of steam when flowing past the stages of the turbine and heterogeneous nucleation caused by impurities. As the pressure of the steam decrease the temperature of the steam also decrease and condensation occur. The source of impurities is mainly from demineralization plant failures and corroded metal in the steam cycle which is carried through to the ACC's. Ingress air provides oxygen and some impurities for the corrosion and nucleation processes. The impurities are carried with these droplets and need to be removed before reaching the ACC.

Preliminary tests before this study at a power station have shown that such droplets can be extracted at the turning vanes in the bend of the steam duct and that the condensate has a much higher impurity concentration than the general condensate in the ACC (Northcott, 2011). The pH of the extracted condensate is lower than those of the condensate in the ACC; therefore, this promotes corrosion of the ACC bundle tubes. Corrosion on the ACC inlet tubes increases maintenance cost on the power station because more polishing of condensate is needed due to the presence of impurities. If the energy used to produce power increases for the same energy output, the efficiency of the power station decreases.

Figure 1.1 illustrates corrosion on the ACC bundles of the power plant. If these droplets can be extracted before reaching the ACC bundles, this corrosion problem can be reduced. Moreover, to polish only this extracted fraction of condensate from impurities instead of all the condensate from the ACC will require a smaller polishing plant, which, in turn, will reduce operating costs. When water is polished, the corrosive products and impurities are removed from the condensate to prevent accumulation of impurities in the cycle (Northcott, 2011).

Pictures were taken of the damaged inlet bundle on Matimba Power Station and one of these pictures is shown in Figure 1.1.



Figure 1.1: Corrosion on entrance to the ACC tubes

Source: Dooley, Aspden, Howell & Du Preez, 2009.

To extract the droplets that cause this bundle to corrode and erode, a water/steam separator needs to be designed. The design should be such that the lowest pressure loss possible through the ducting would be caused by the separator. The placement of this separator in the ducting must also be strategic to extract most of the liquid it can. The shape of the separator and the amount of liquid colliding with the vanes in the bend of the ducting is important factors in this study.

A few basic shapes are evaluated through computational fluid dynamics (CFD) using ANSYS FLUENT version 14.0. The shape with the most aerodynamic performance for the type of flow present in the ducting is then optimized to reduce pressure loss. An airfoil shape is determined as the most aerodynamic shape of all. Sensitivities on the radius ratio of the elliptical section of the airfoil is done and also on the length of the tail of the airfoil. The most efficient placement of the separator onto the vane determined by moving the separator forward and backwards onto the vane. Lastly a simulation is done on each vane to see how big the pressure loss would be if a pipe shaped separator is used on each vane separately. A pipe is commercially available in abundance and would be an easy

and inexpensive modification to the plant. This section is just for informational purposes. From this it can be seen that the effect on pressure of such a small separator is very small in comparison with the total pressure in the duct.

To know which vane in the bend of the ducting is the best location for extracting most of the liquid, the droplet size distribution should be known. There is no information regarding the droplet size range on the power station so the range is determined only numerical. The upper limit and lower limits are determined by comparing the results of a number of simulations. Limits are reached where the value of certain parameters does not change anymore and won't have a significant influence on the end results.

The droplets identified stays spherical mostly in this type of flow conditions with some minor difference in results when the larger droplets are simulated. External forces like gravity, Saffman's lift forces and Magnus forces also have an insignificant effect on the end results since a large portion of the identified droplet size range is in the Stokes flow region where droplets follow the fluid flow closely.

Water liquid is accumulated at the bottom of the duct, which suggests that there is liquid film present on the walls of the duct (Northcott, 2011). The liquid film on the duct walls and vanes can entrain droplets when the droplets collide with the walls in the duct. If a droplet does not possess enough energy to escape the liquid film during impact, the droplet will stick to the wall.

Design conditions for the duct were taken into consideration, using the LPT outlet mass flow of 204 kg/s as the duct inlet boundary condition together with the ACC inlet total pressure of 19.8 kPa as the duct outlet boundary condition. The steam flow had 5 % wetness at 60 °C operating in a steady state. A steady-state $k-\omega$ model was used for this study because it is more forgiving than the $k-\epsilon$ model against walls when the boundary layer is not solved.

Because of the low volume fraction occupied by the droplets, which is less than 10 %, discrete phase modelling could be selected to simulate the two-phase flow field. Since the density of liquid is higher than the density of vapour, the volume fraction will be less than the mass fraction of 5 %. When droplet particles are injected into a steam flow, it has to be known what influence the droplets will have on each other and on the steam flow field. When the volume fraction of the secondary phase is less than 10 %, particle-particle interaction can be neglected. The interaction and effects of the volume fraction of particles on the continuous phase can be neglected when the discrete phase model (DPM) is used (ANSYS, 2012). An uncoupled discrete phase model injection is thus used in this project. In the discrete phase model, the continuum is solved with Navier-Stokes equations and the particles are solved by Lagrangian particle tracking through the calculated flow field.

For future studies the droplet sizes can be sampled by using laser diffraction techniques, which can sample nanometre droplet sizes. The cost of such equipment can be very high, however, and the need for using such techniques at the power plant should be evaluated carefully. The investigation and evaluation of the need for this equipment and obtaining permission to procure it are a time-consuming process.

CHAPTER 2

RATIONALE

A test was conducted at Matimba Power Station before this study was conducted to establish whether liquid extraction from one of the vanes in the bend of the steam duct was possible and to establish how much liquid could be extracted. The impurity level of this water was analysed, and it was concluded that the level of impurities in this extracted liquid was much higher than the liquid condensed in the ACC, as shown in Table 2.1 below. The pH of this extracted liquid was also lower than the pH of condensate in the ACC, which promotes corrosion to the bundle tubes. Figure 2.1 shows an aerial view of the power station.



Figure 2.1: Aerial view of Matimba Power Station

Source: Dooley et al., 2009.

From Figure 2.1 the six Matimba units and the ACC in the form of A-frames can be seen clearly. A-frames increase the contact area of the condenser with the ambient air and is using less space than what a flat area would've consumed.

Table 2.1: Laboratory results Unit 6 ACCCT/ACC duct – samples 17 and 18 Jan 2011

17 Jan 2011		
Parameter	Unit 6 ACCCT	LP2 ACC horizontal duct
Turbidity	2.07	10.09
pH	9.02	6.46
K25 $\mu\text{S}/\text{cm}$	11.00	4.02
Chloride (ppb)	2.86	22.43
Sulphate (ppb)	16.85	92.74
Sodium (ppb)	*	*
Silica (ppb)	6.02	92.74
18 Jan 2011		
Parameter	Unit 6 ACCCT	LP2 ACC horizontal duct
Turbidity (NTU)	*	*
pH	9.52	8.81
K25 $\mu\text{S}/\text{cm}$	10.56	3.28
Chloride (ppb)	2.51	16.20
Sulphate (ppb)	0.71	171.87
Sodium (ppb)	2.23	5.17
Silica (ppb)	10.47	39.44

Source: Northcott, 2011.

2.1 Test setup

Drawings A.1 and A.2 in Appendix A show the geometry of the duct, with guide vanes and the vanes in the bends, respectively. The hole in the middle of the bend, between the vanes, represents the location of the bypass and is only present at the first bend. Figure 2.2 shows the layout of the steam cycle from the LPT outlet to the ACC. The bend just below V1 is termed ‘bend 1’, and the one below V2 is

characterised as ‘bend 2’. V1 receives the steam from the LPT, and the steam is transported through the duct to H3, which feeds the ACC tubes. The rectangular structure around the duct is the part simulated in this study, and the surrounded part indicates where the separator was installed.

Separating liquid droplets means separating the steam and droplets from each other by using the inertia of the droplets. As the steam is forced to change direction in the bend, large droplets will flow downward and collide with the vane, from where they can be extracted.

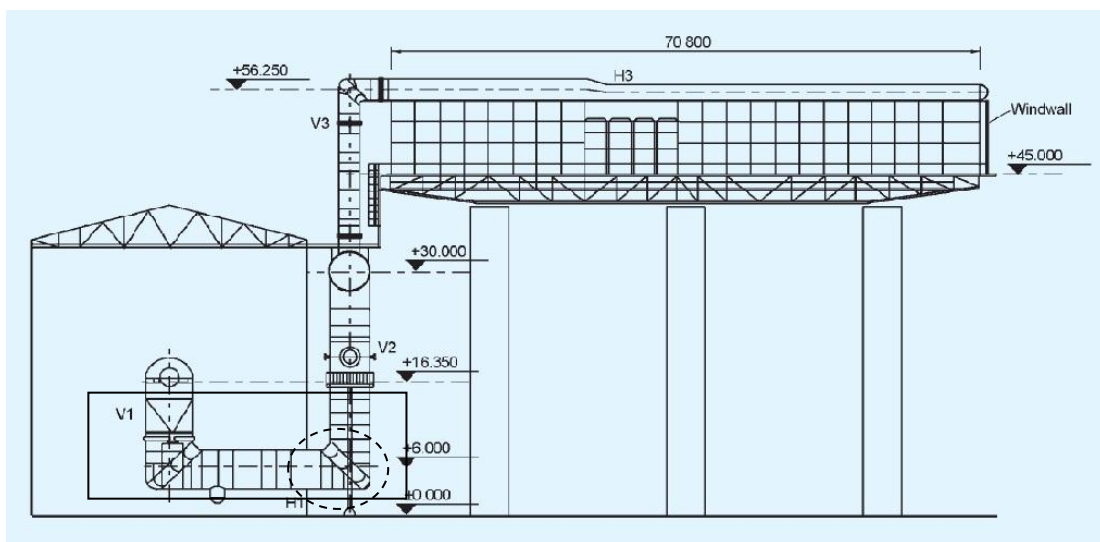


Figure 2.2: Side view of the ACC ducts.

Source: Dooley et al., 2009.

Figure 2.3 (a) shows the location of the separator in the second bend of the duct, and (b) shows the geometry of the separator used to extract the liquid. The white arrow in (a) indicates where the separator was installed during testing. The separator has a diameter of 37.5 mm and is used this separator is simulated in the last section of this study.

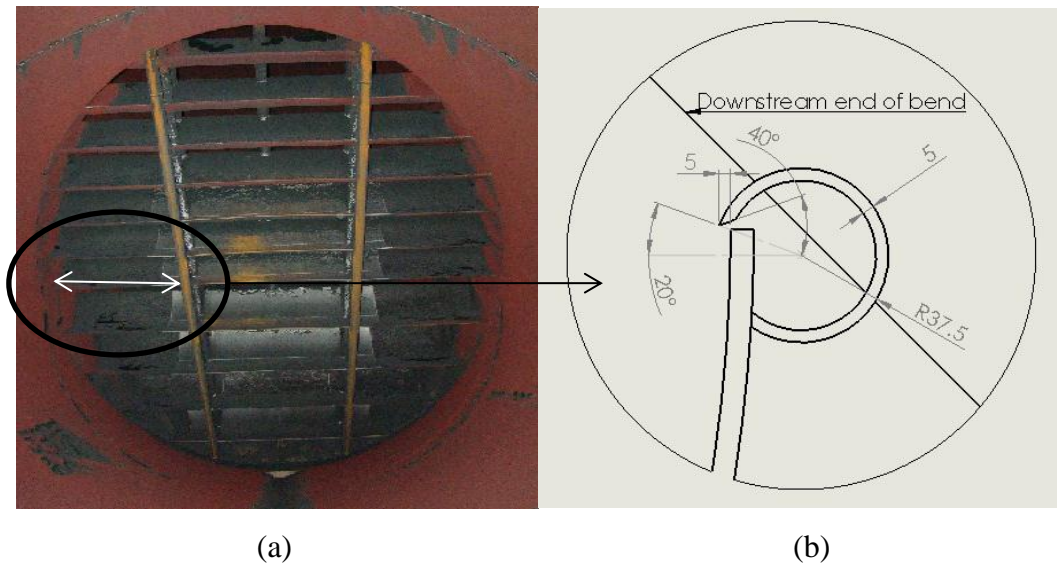


Figure 2.3: Here (a), left, shows the location and length of the separator at the downstream side of the bend, surrounded in Figure 2.2, while (b) is a detailed sketch of the separator welded onto the trailing edge of the vane viewed from the side.

The shape of this separator is optimized further in this thesis. Although a pipe is the easiest and most inexpensive way for doing a modification on the power plant, some other shapes is going to be suggested if the need for such an aerodynamic shape separator is required.

2.2 Test results

Table 2.2 show the results of the amount of liquid extracted in one-minute intervals, and the rate at which liquid was extracted. After 10 minutes had passed, the total extracted volume of 8.26 l liquid was divided by 10 minutes to provide the average extraction rate of 0.826 l/min. The duration of the liquid extraction test, amount of liquid extracted, volume flow rate of extracted liquid, average electrical load, average back pressure, ambient air temperature and ACC duct temperature was monitored during testing and the results is shown is Table 2.2 (Northcott, 2011).

Table 2.2: Results of liquid extracted during preliminary testing

Duration (min)	Volume (l)	Extraction rate (l/min)	Average electric load (MW)	Average back pressure (kPa)	Ambient air temp (°C)	ACC duct temp (°C)
1	0.86	0.86	665.22	24.516	21.44	65.12
2	1.64	0.82	665.56	24.757	21.43	65.30
3	2.54	0.85	668.53	24.250	21.35	64.90
4	3.54	0.89	665.09	24.372	21.37	64.95
5	4.82	0.96	666.85	24.507	21.32	65.05
6	5.36	0.89	667.11	24.301	21.60	64.85
7	6.10	0.87	666.65	24.922	21.92	65.38
8	7.30	0.91	666.91	25.474	22.25	65.87
9	7.54	0.84	666.60	25.896	22.39	66.35
10	8.26	0.83	666.01	26.317	22.57	66.73

Source: Northcott, 2011.

2.3 Discussion and conclusion of the test setup

It was experimentally proved that liquid could be extracted from the guide vanes and that the droplets were of sufficient size to be extracted using their inertia to separate them from the steam or by sticking to the liquid film existing on the vanes in the bend of the duct. A CFD model can be used to design the separator more aerodynamic to reduce the pressure loss caused by the separating object in the flow path of the steam. Because the droplet size during this test is not available, assumptions regarding this size have to be made and can be predicted numerically.

CHAPTER 3

LITERATURE STUDY

Before the CFD model can be simulated there must be finalization on some models and inputs. To determine the best location for the separator it should be known where most of the droplets would be. Therefore the correct drag law has to be determined and the external forces working on the droplets should be known to predict their trajectories. Basic shapes for an aerodynamic separator should also be identified.

3.1 Turbulence model

To select a model with the appropriate governing equations, the Reynolds number (Re) of the flow domain should be known. If the Reynolds number of a flow field is smaller than or equal to 2 300, the flow is laminar. If the Reynolds number is more than or equal to 10 000, the flow is turbulent and the unspecified region for the value of the Reynolds number is the transitional region (Kröger, 1998). Equation 3.1 measures the relation between the inertia and viscous forces of the flow and Equation 3.2 calculates the mixture average velocity.

$$Re = \frac{\rho_m u_m D}{\mu_m} \quad (3.1)$$

$$u_m = \frac{\dot{m}}{\rho_m A} \quad (3.2)$$

Here u_m , ρ_m , μ_m , \dot{m} , D and A are the mixture average velocity, combined density, combined dynamic viscosity, total mass flow, diameter of the duct and area of the duct, respectively.

The total mass flow of the two-phase steam was 204 kg/s at 19.8 kPa absolute pressure and temperature of 60 °C. The average velocity and Reynolds number of

the mixture were calculated as in the region of 76 m/s and 4.5×10^6 , respectively, which indicated fully turbulent flow.

When selecting the turbulence model, it is of importance to take computational effort and cost in terms of central processing unit time and accuracy into account. The central processing unit time for simulations is virtually linearly related to the number of cells used and the number of equations that have to be solved.

Because of hardware capability and licensing, an economic general model has to be selected, which will give accurate results within a reasonable time by taking into account a large Reynolds number with a large geometry. The duct diameter in the study was 4.988 m.

Reynolds-averaged Navier-Stokes (RANS) turbulence models are the most economic approach for computing complex turbulent industrial flows and are time averaged. They use the Boussinesq approximation whereby the Reynolds stresses are solved proportionally to the mean velocity and the eddy viscosity is calculated. Although Reynolds stress models (RSMs) are part of the RANS family and although they can predict flows with significant body forces, they consume much more computing time than the RANS models because more equations need to be solved (one equation for each of the six independent Reynolds stresses) and do not always justify claims of increased accuracy. Large-eddy simulation (LES) models can also be used for more accurate results (complex geometries) but require excessively high resolution for wall boundary layers and computation time. With the LES model, enhanced wall treatment is used and the mesh at the wall has to be very fine (Versteeg, 2007).

There are six RANS models to choose from: the Spalart-Allmaras model, the standard $k-\epsilon$ model, the renormalisation group (RNG) $k-\epsilon$ model, the realisable $k-\epsilon$ model, the standard $k-\omega$ model and the shear-stress transport (SST) $k-\omega$ model.

3.1.1 Spalart-Allmaras model

This model, which has one extra transport equation for eddy viscosity and an algebraic equation for length scale, provides economical computations of boundary layers in external aerodynamics. This model is not recommended for general industrial purposes due to the inaccuracy of results in the absence of solid boundaries (ANSYS, 2012).

3.1.2 k- ϵ Models

These models have two extra transport equations for turbulence kinetic energy (k) and its viscous dissipation rate (ϵ) and model the Reynolds stresses using the eddy viscosity approach. For a wide range of turbulent flows, the standard k- ϵ model shows robustness, economy and reasonable accuracy; however, this model has poor performance in adverse pressure gradients and boundary layer separation, which is the case for all the k- ϵ models. It uses wall functions (log law), and the log law is based on flow over a flat plate. The k- ϵ models predict a delayed and reduced separation of the flow field, and the near-wall performance is unsatisfactory for boundary layers with adverse pressure gradients.

The RNG and realisable k- ϵ models are improvements in accuracy on the standard k- ϵ model, especially for rotational and swirling flows, but at a computational time expense. For the RNG model, an additional term in its ϵ equation is added for accuracy of rapidly strained flows. The realisable k- ϵ model contains alternative formulation to satisfy mathematical constraints (physics on turbulent flows) on the Reynolds stresses and uses wall functions.

3.1.3 k- ω Models

The k- ω models are more adept at predicting adverse pressure gradient boundary layer flows and separation but are extremely sensitive to the solution, depending on the free-stream values of k - and ω - outside the shear layer. In the flow

encountered in the study, there was no free stream; therefore, this restriction was not of importance. There are two $k-\omega$ models, namely the standard $k-\omega$ model and the SST $k-\omega$ model, which is a modified standard $k-\omega$ model.

The SST $k-\omega$ model avoids the free-stream sensitivity of the standard $k-\omega$ model by combining elements of the ω -equation and the ε -equation. Not only does this model compute flow separation from smooth surfaces (vanes) more accurately than the $k-\varepsilon$ models but it also does more accurate computation of the boundary layer details than the Spalart-Allmaras model. It also uses the enhanced wall treatment as default.

In the SST $k-\omega$ model, the robust and accurate formulation of the standard $k-\omega$ model in the near-wall region is blended with the free-stream independence of the standard $k-\varepsilon$ model in the far field. The standard $k-\varepsilon$ model converts to the standard $k-\omega$ model in this process.

The standard $k-\omega$ model and the transformed $k-\varepsilon$ model are both multiplied by a blending function and then summed. This blending function, which is designed to be in the near-wall region, activates the standard $k-\omega$ model and becomes closer to zero as the flow moves away from the surface, which activates the transformed $k-\varepsilon$ model. The drag on the droplets is more important than the shear against the walls (pressure drop) in this case because the flow pattern will predict the trajectories of the droplets and, consequently, it is not necessary to increase calculation time by using enhanced wall treatment. The boundary layer is a small part of the flow, and the flow pattern needs to be more or less right.

The SST model incorporates a damped cross-diffusion derivative term in the ω equation to perform this refinement on the $k-\omega$ model. To account for the turbulent shear stress, the definition of the turbulent viscosity (μ_t) is modified and the modelling constants are different.

Table 3.1: RANS turbulence model comparison

Model	Accuracy	Time	Accurate in absence of solid boundaries	Stability at boundaries	Accurate flow separation
Spalart- Allmaras	yes	yes	no	yes	yes
Standard k-ϵ	yes	yes	yes	no	no
RNG	yes	no (mesh has to be too fine at boundaries)	yes	yes	no
Realisable k-ϵ	yes	yes	yes	no	yes
Standard k-ω	yes	yes	yes	yes	yes
SST	yes	yes	yes	yes	yes
RSM	yes	no	yes	yes	yes
LES	yes	no	yes	yes	yes

In Table 3.1, it can be seen that there is very little to choose between the k- ϵ models and k- ω models. The aim is to construct the flow pattern in order to calculate particle trajectories. More attention needs to be given to drag than shear, which indicates changes in flow direction are important. This means that the boundary layer does not have to be solved in such detail, which will significantly increase computation time. The boundary layer is a small part of the flow, as mentioned before, and the large droplets, which are the ones that can be extracted through separation due to their larger inertia, will punch through the boundary

layer. Therefore, a fine mesh on the wall and enhanced wall treatment will not be necessary due to the significantly increased computation time needed.

Since there were two models to choose from, the standard $k-\omega$ model and not the SST model was chosen because this model has fewer terms, which increases simulation stability.

After a turbulence model for the primary fluid phase had been identified, a secondary phase model could be identified.

3.2 Euler-Lagrange and Euler-Euler approaches

There are two models to choose from with regard to the two-phase flow simulations, namely the Euler-Lagrange approach and the Euler-Euler approach.

In the Euler-Lagrange approach, the fluid phase is treated as a continuum by solving the Navier-Stokes equations, while the dispersed phase is solved by tracking a large number of droplets through the flow field. The particle-particle interactions can be neglected when the volume fraction of the dispersed phase is less than 10 %, and this will significantly simplify the computation process.

In the Euler-Euler approach, the different phases are treated as interpenetrating continua. One phase cannot be occupied by the other as each phase has its own set of conservation equations.

Since the volume fraction of the dispersed phase was less than 10 % and to save computation time, the Euler-Lagrange approach was deemed more appropriate for this study (ANSYS, 2012). To use this model, droplet size and distribution needed to be established.

3.3 Discrete phase modelling

Droplets are released from the inlet of the flow domain to represent the liquid phase in the two-phase flow field. The fluid phase is treated as a continuum by

means of the Eulerian approach, by solving the Navier-Stokes equations, while the dispersed phase is solved by Lagrangian particle tracking. For uncoupled (one-way) simulations, the droplet trajectories are computed individually, at specified intervals, at the end of the simulation. The droplets have no influence on the pressure drop on the steam side when the model is uncoupled. In this approach, particle-particle interaction can be neglected since the dispersed phase occupies a low volume fraction of 0.00067 %. During discrete phase modelling, one droplet parcel is released from the centre of each cell at the inlet boundary.

Equations of motion for droplets

The trajectories of the particles are calculated by integrating the force balances on those particles. This force balance equates the particle inertia with the forces acting on the particles. This balance is written in the x-direction in the Cartesian coordinate system (ANSYS, 2012).

$$\frac{du_p}{dt} = F_D (u_f - u_p) + \frac{g (\rho_p - \rho_f)}{\rho_p} \quad (3.3)$$

Here, u_f is the steam velocity, u_p the droplet velocity, ρ_p the density of the droplet, ρ_f the density of the steam and $F_D (u_f - u_p)$ the drag force per unit particle mass. In the operating conditions, g (gravity acceleration force) was specified as 9.81 m/s^2 downwards to the surface of the earth, in the y-direction. It is now apparent that

F_D can be calculated by

$$F_D = \frac{3\mu C_D Re}{4 \rho_p d_p^2} \quad (3.4)$$

and Re by

$$Re \equiv \frac{\rho_f d_p |\vec{u}_f - \vec{u}_p|}{\mu_f} \quad (3.5)$$

Here, d_p is the diameter of the particle, μ_f the molecular viscosity of the fluid, Re the relative Reynolds number and C_D the drag coefficient.

To track a particle through the flow field, the drag on the droplets should be known.

3.4 Drag laws

The drag coefficient on the droplets plays a fundamental role in prediction of the motion of the particle flow. The spherical drag law (SDL) is used for particles that retain their spherical shape throughout the simulation. As droplets start to deform the dynamic drag law (DDL) can be used.

First it should be known what the relative velocity is between the steam and the droplets which are used to determine the external forces working on the droplet. The terminal velocity of droplets will be a good indication of what the relative velocities in the duct will be since the terminal velocity is the velocity of the droplets relative to the fluid. This terminal velocity in the vertical direction can be calculated by setting the drag force (F_D) equal to force on a droplet falling under gravity ($m_p g$).

$$F_D = \frac{1}{2} \rho_f u_r^2 A_p C_D = m_p g \quad (3.6)$$

Here m_p is the mass of the droplet and A_p the cross sectional area of the droplet. The drag coefficient past a smooth sphere is

$$C_D = \frac{24}{Re_p} = \frac{24 \mu_f}{\rho_f d_p u_r} \quad (3.7)$$

By manipulation of Equation 3.6 and 3.7 the relative velocity simplifies to

$$u_r = \frac{m_p g}{3 \mu_f \pi d_p} = \frac{V_p \rho_p g}{3 \mu_f \pi d_p} \quad (3.8)$$

For a 500 μm particle u_r calculates to

$$u_r = \frac{6.54 \times 10^{-11} \times 983 \times 9.81}{3 \times 1.11 \times 10^{-5} \times \pi \times 500 \times 10^{-6}} = 12.07 \frac{\text{m}}{\text{s}} \quad (3.9)$$

Now that the relative velocity is known it can be calculated if droplet breakup will occur. As droplets flow through the ducting, the droplet experiences aerodynamic forces and the surface tension of the droplet is the force that holds the droplet in its spherical shape. As the relation between the aerodynamic forces and the viscous forces (surface tension) increases, the shape of the droplet will start to change from a spherical shape to a disk shape, and with further increases in this relation, the droplet will experience breakup. An appropriate model should be selected using the average droplet size, conditions and properties as indicators.

Stochastic secondary droplet model

This model is suitable for moderate to high Weber number applications and treats the droplet breakup as a discrete random event, resulting in a distribution of diameter scales over a range. The secondary droplet size after breakup is sampled from an analytical solution of the Fokker-Planck equation for the probability distribution. The size distributions of the particles are based on local conditions.

If $We > We_c$, droplet breakup will occur where We_c is the critical Weber number. This number indicates that the surface tension of the droplet, which provides the internal forces to form the droplet, is still sufficient in relation to the external aerodynamic forces acting on it. This number can be calculated by

$$We_c = 12 (1 + 1.077 On^{1.6}) \quad (3.10)$$

with

$$On = \frac{\mu_p}{\sqrt{\rho_p d_p \sigma}} \quad (3.11)$$

where On is the Ohnesorge number, and when $On < 0.1$, the droplet viscosity may be neglected and $We_c = 12$, which is shown in Figure 3.1 (Tarnogrodzki, 1992). The x-axis is shown in the logarithmic scale from 1 μm to 500 μm .

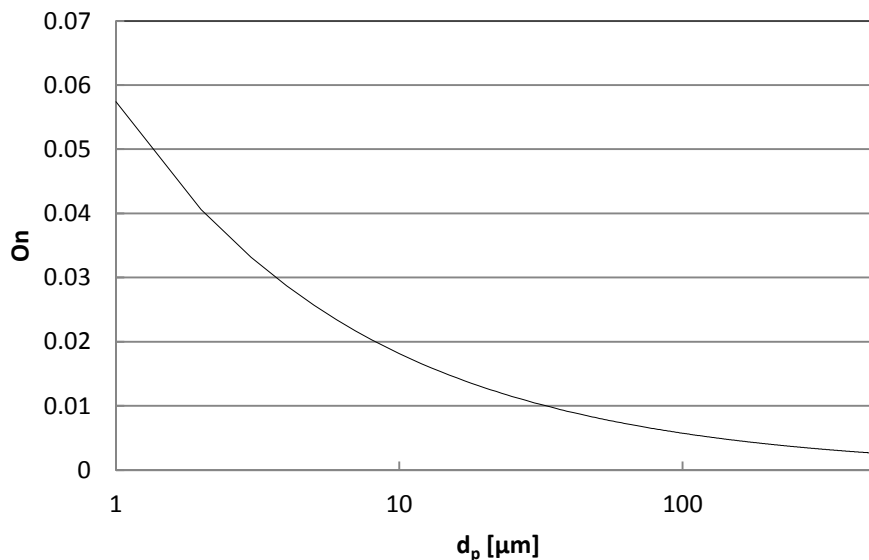


Figure 3.1: Ohnesorge number for different sizes of droplets

Figure 3.1 shows that the smaller the droplet is the larger the Ohnesorge number. The critical Weber number for all droplets in Figure 3.2 will be 12. The Weber number for the droplets can be calculated by

$$\begin{aligned} We &= \frac{\rho_f u_r^2 d_p}{\sigma} = \frac{0.13 \times 12.07^2 \times 500 \times 10^{-6}}{0.0662} \\ &= 0.143 \end{aligned} \quad (3.12)$$

where $\sigma = 0.0662$. N/m is the surface tension of saturated water at 19.8 kPa (Kröger, 1998). The Weber number gives the relationship between the continuous fluid stresses and the surface stresses. Figure 3.2 shows the Weber numbers of the droplets up to 500 μm and it can be seen that it is far from the value of 12 which is the critical Weber number for all sizes. Droplets will thus not breakup

theoretically and since this value is so far from 12 no big fluctuations on the shape of the droplet can also be expected. Since a 500 μm droplet has a Weber number in the region of 0.14 no breakup will occur. In some cases at severe changes in flow direction the relative velocity might be larger than its terminal velocity and some deformation of the shape of the droplet can be expected as the Weber number approaches 12. For a 500 μm droplet to break up the relative velocity should be in the region of 110 m/s so breakup in the CFD model is not expected.

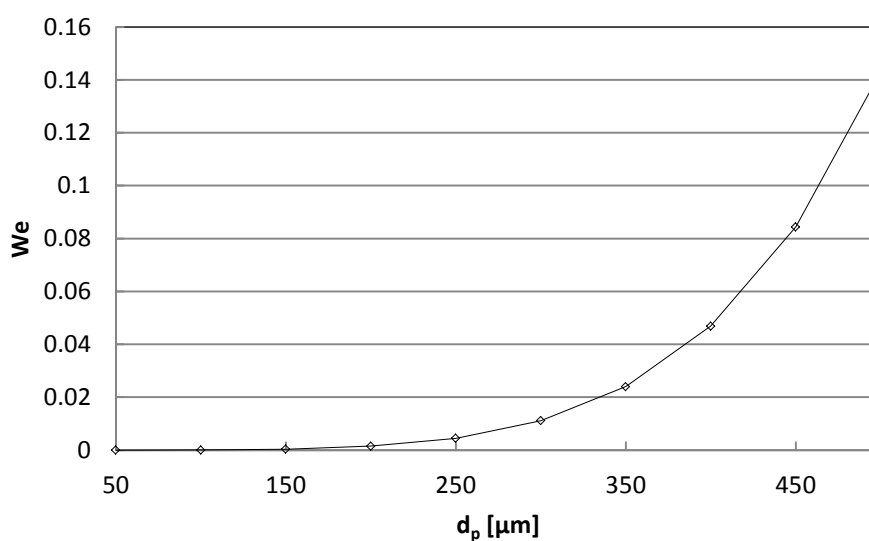


Figure 3.2: Weber numbers for droplets ranging from 50-500 micron

It can be seen that the Weber number of the droplets increase as the droplet size increase.

3.5 Stokes number

The Stokes number (Stk) gives an indication of how the droplets will behave in the steam flow field, according to the ANSYS Theory Guide (2012). It is the relation between the particle response time (τ_d) and the system response time (t_s). If $Stk \ll 1$, the particle will follow the fluid flow closely, and if $Stk > 1$, the particle will move independently of the flow field. The discrete phase model can be used in both cases. This number can be calculated by the following equation:

$$Stk = \frac{\tau_d}{t_s} \quad (3.13)$$

where

$$\tau_d = \frac{\rho_d d_p^2}{18 \mu_f} \quad (3.14)$$

and

$$t_s = \frac{L_s}{u_r} \quad (3.15)$$

where L_s is the characteristic length which for internal flows is the hydraulic diameter of the duct (ANSYS, 2012). For a 500 μm droplet the Stokes number simplifies to

$$Stk = \frac{\rho_p d_p^2 u_r}{18 \mu_f L_s} = \frac{983 \times (500 \times 10^{-6})^2 \times 12.07}{18 \times 1.11 \times 10^{-5} \times 4.988} = 2.975 \quad (3.16)$$

Figure 3.3 shows the Stokes number for droplet sizes ranging from 50 μm to 500 μm . It can be seen that the Stokes numbers are relatively small and droplets will follow the fluid flow closely. Droplets larger than 350 μm have Stokes numbers higher than 1 and will tend to deviate from the flow field. Droplets \ll 350 μm will follow the fluid flow closely. This theory will enable to select a minimum size range of droplets for the CFD model since a point will be reached where the decreasing of droplet sizes in the simulation will make no difference in results. Also this theory predicts that an upper limit for the droplet size range will be reached where no difference in results will occur as the droplet size increases.

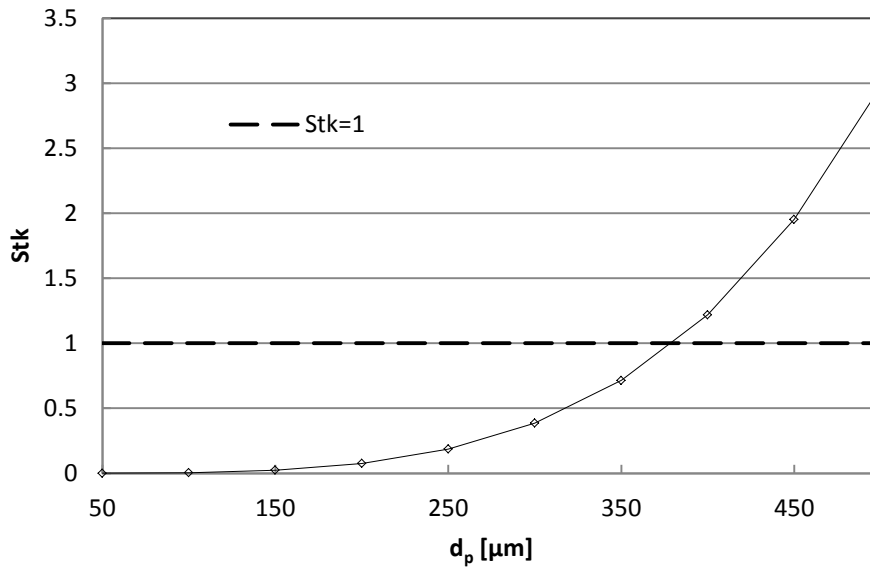


Figure 3.3: Stokes numbers for droplet sizes ranging from 50 to 500 μm

3.6 Lift forces

While droplets flow through the duct, they can experience Saffman's lift forces, due to shear, and Magnus forces, due to rotation of droplets that influence their flow path. No significant Magnus or Saffman's forces can be expected when particles are following the fluid flow closely (Van Thienen, Vreeburg & Blokker, 2010).

The Magnus force is generated when there is a difference in rotational velocity between the droplet and the fluid. When a droplet is moving slower than the fluid and rotates towards the wall at a rate slower than the surrounding fluid, the Magnus force is directed towards the wall of the duct. When the droplet's rotational velocity is faster than the surrounding fluid's rotational velocity or when the droplet is moving faster than the fluid, the Magnus force is directed towards the centre of the duct. In the event that both the rotational and the local velocity of the droplet are greater than that of the fluid, the Magnus force is directed towards the wall (Van Thienen et al., 2010).

When the droplet and the fluid have a velocity differential and when the fluid has a velocity gradient perpendicular to the direction of motion of the droplet, the Saffman's lift force is generated by shear. When the droplet is moving faster than the fluid, the Saffman's force is directed to the wall. When the droplet is moving slower than the fluid, the Saffman's force is directed towards the centre of the duct (Van Thienen et al., 2010).

To determine if these forces are going to have a big influence on the trajectories of the droplets, they can be compared against the force of gravity. The gravitational force (F_G) experienced by a 500 μm droplet is a function of its size and relative density:

$$\begin{aligned}
 F_G &= \frac{\pi}{6} d_p^3 (\rho_p - \rho_f) g \\
 &= \frac{\pi}{6} \times (500 \times 10^{-6})^3 \times (983 - 0.13) \times 9.81 \\
 &= 6.31 \times 10^{-7} N
 \end{aligned} \tag{3.17}$$

The magnitude of the Saffman lift force F_S scales linearly, with the differential velocity u_r between the particle and the surrounding fluid:

$$\begin{aligned}
 F_S &= 1.62 \sqrt{\mu_f \rho_f} d_p^2 u_r \sqrt{\frac{du}{dy}} \\
 &= 1.62 \times \sqrt{1.11 \times 10^{-5} \times 0.13} \times (500 \times 10^{-6})^2 \times 12.07 \times \sqrt{12.07} \\
 &= 2.04 \times 10^{-8} N
 \end{aligned} \tag{3.18}$$

Here $\frac{du}{dy}$ is the radial velocity of the fluid in the y-direction and is also assumed to be the value of relative velocity.

The magnitude of the Magnus force, like that of the Saffman lift force, is a linear function of the differential velocity between the particle and the surrounding fluid velocity u_r :

$$\begin{aligned}
 F_M &= \frac{\pi \rho_f}{8} d_p^3 u_r \left(\omega - 0.5 \frac{du}{dy} \right) \\
 &= \frac{\pi \times 0.13}{8} \times (500 \times 10^{-6})^3 \times 12.07 \times (209 - 0.5 \times 12.07) \\
 &= 1.56 \times 10^{-8} N
 \end{aligned} \tag{3.19}$$

Here ω is the differential rotational velocity between the droplet and the surrounding fluid and is assumed to be 209 rad/s (2000 rpm) which is extremely high. The reason why such a large value is selected is to emphasize the influence of the force in comparison with other forces. For all three forces the relative velocity and radial velocity is assumed to be equal to the terminal velocity of the droplet. Figure 3.4 show the results of these forces on a 500 μm droplet. As the size of the droplet increases, the forces on the droplet increases and so the largest droplet in the range established later in this thesis is used to determine the effect of these forces.

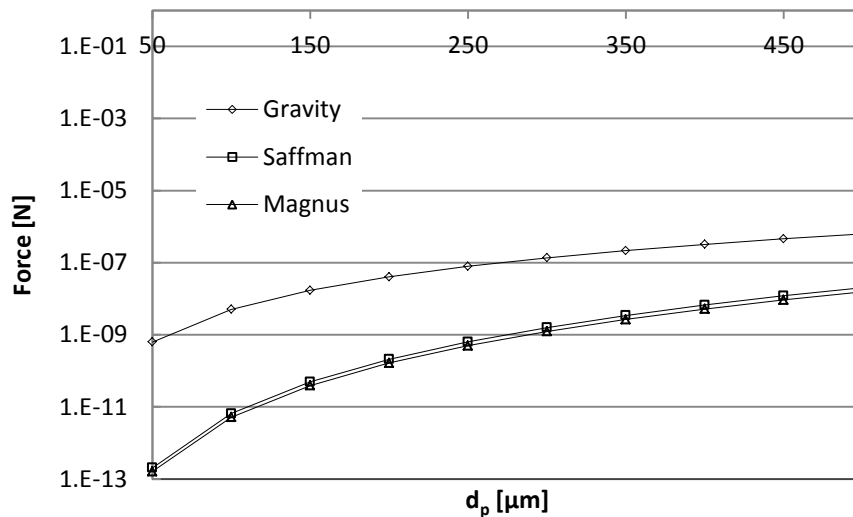


Figure 3.4: Gravitational-, Saffman- and Magnus forces on droplets that are ranging from 50-500 μm

From these results it can be seen that gravity will have the biggest effect on the droplet trajectory and then the Saffman's force by a small margin.

3.7 Wall film model theory

Water accumulates at the bottom of the duct, thus there is a wall film present on the walls of the duct. The water found in this area plays a big role in the droplet-wall interactions.

The Eulerian wall film model predicts the creation and flow of thin liquid films on the surface of walls. For example, while driving a vehicle in rainy weather, this film can be found when raindrops become affixed to the windscreen. These droplets start to form thin films on the windscreen and move faster when the vehicle's speed increases. As the droplets collide with the wall of the duct, thin films form. The main assumptions and restrictions for the wall film model are that the film particles are in direct contact with the wall and that the simulation is transient.

Interaction during impact with a boundary

When a droplet collides with the wall film, there can be four different outcomes. The droplet can rebound from, stick to, splash against or spread on the wall. The dimensionless impact energy E of impingement indicates when a droplet will stick to the wall and is defined by

$$E^2 = \frac{\rho_l u_r^2 d_p}{\sigma} \left(\frac{1}{\min(h_0/d_p, 1) + \delta_{bl}/d_p} \right) \quad (3.20)$$

where ρ_l is the liquid density, u_r is the relative velocity of the droplet in the reference frame of the wall (i.e. $u_r^2 = (u_p - u_w)^2$, where $u_w = 0$ because the wall is stationary and $u_p = 76 \frac{m}{s}$, which is the average inlet velocity of the duct), h_0 is the film height and δ_{bl} is the boundary layer thickness defined by

$$\delta_{bl} = \frac{d_p}{\sqrt{Re}} \quad (3.21)$$

with

$$Re = \frac{\rho_l u_r d_p}{\mu_l} \quad (3.22)$$

For a 500 micron droplet

$$Re = \frac{983 \times 76 \times 500 \times 10^{-6}}{4.63 \times 10^{-4}} = 80\,678 \quad (3.23)$$

$$\delta_{bl} = \frac{500 \times 10^{-6}}{\sqrt{80\,678}} = 1.76 \times 10^{-6} \quad (3.24)$$

$$E = \sqrt{\frac{983 \times 76^2 \times 500 \times 10^{-6}}{0.0662} \times \left(\frac{1}{\frac{100 \times 10^{-6}}{500 \times 10^{-6}} + \frac{1.76 \times 10^{-6}}{500 \times 10^{-6}}} \right)}$$

$$= 459 \quad (3.25)$$

Here the droplet diameter is larger than the film thickness. Since the velocities of droplets against the wall vary, the average duct inlet velocity was used to give an indication of the distance from the low impact energy region.

When $E < 16$, the particle velocity is set to the wall velocity and the particle will stick. Figure 3.5 shows the dimensionless impact energy of different sizes of droplets for different film heights moving at 76 m/s because this is the average steam velocity in the duct. When droplets are smaller than 3 μm they will adhere to the wall for all film heights. There is no difference in droplet entrainment results for liquid films smaller than 300 μm but the larger the ratio of the droplet size to the liquid film gets the more the entrainment results deviate. For the selected range for all droplets $E < 16$ for any film height when droplets are larger

than 3 μm and the graphs overlay each other when droplets is smaller than 3 μm so any film thickness can be selected for this study.

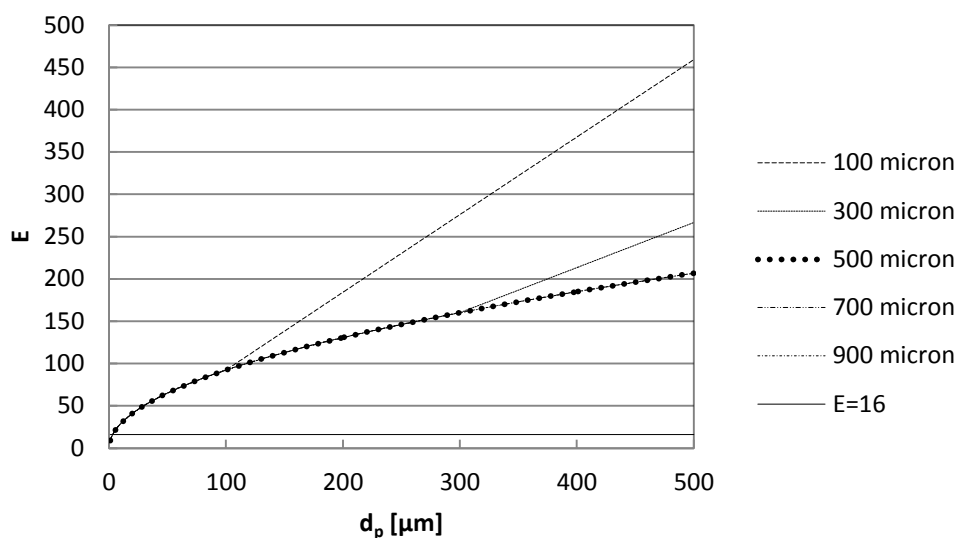


Figure 3.5: Dimensionless impact energy for different liquid film heights for droplet sizes between 1 and 500 μm with a relative velocity of 76 m/s

3.8 Shape effects on drag

To design a separator which will cause the least pressure drop in the duct, the most aerodynamic shape has to be determined. Figure 3.6 shows five basic shapes that can be evaluated which are used for different applications in the industry. The drag coefficient of these shapes is shown and was tested in a low speed wind tunnel but will still be a good indicator for the amount of pressure loss the shape will cause if used in the turbulent duct. The values shown here for the drag coefficient were determined experimentally by placing models in a low speed (subsonic) wind tunnel and measuring the amount of drag, the tunnel conditions of velocity and density, and the reference area of the model (NPARC, 2015). From Figure 3.6 it is shown that an airfoil shape has the smallest drag coefficient under the low speed conditions with a small margin over the spherical shape. A flat plate and prism have the largest drag coefficient. All these shapes are going to be evaluated for the turbulent conditions in the next chapter.

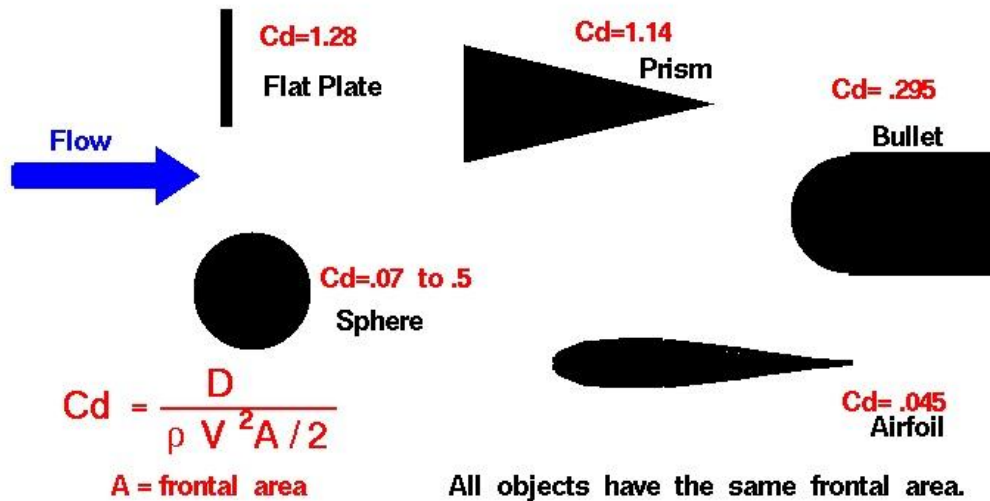


Figure 3.6: Drag on different objects with aerodynamic shapes

Source: NPARC, 2015.

The drag coefficient is a number which engineers use to model all of the complex dependencies of drag on shape and on flow conditions. The projected frontal area of each object was used as the reference area.

The effect of shape on drag can be evaluated by comparing the values of drag coefficient for any two objects as long as the same reference area is used and the Reynolds number is matched. These drag coefficients were measured in a low speed wind at the same Reynolds numbers. The shapes in Figure 3.6 are evaluated later in the section on turbulent flow.

CHAPTER 4

COMPUTATIONAL FLUID DYNAMICS MODEL

Theoretically it can be proved that condensate can be extracted from steam through water/steam separation. Particle tracking is validated for the model where analytical results is compared to numerical results by doing calculations for a droplet falling vertical under the force of gravity. After the validation process a grid independence study is conducted on the flow domain in the duct from where the droplet size range is established. Different submodels need to be simulated to test the application of certain models, such as the DDL, external forces working on the droplets and Eulerian wall film model. When the input parameters for the flow field are established, the location to place a separator can be determined. Lastly a design can be done on an aerodynamic separator.

4.1 Validation of the model

The discrete phase model is validated by doing an analytical calculation on a free falling droplet. The analytical solution of the terminal velocity of this droplet is then compared to the numerical CFD solution.

To validate the DPM a droplet falling under the force of gravity a 100 μm droplet is dropped in a 1 m long two dimensional domain with a width of 0.1 m and the droplet's downward velocity increased till it reached its terminal velocity. Firstly an analytical solution is obtained where the terminal velocity of the droplet is calculated from where this solution is compared to the numerical solution.

Analytical solution

To calculate the terminal velocity (u_t) of a droplet the drag force on the droplet is set equal to the gravitational force of the droplet.

$$F_D = \frac{1}{2} \rho_f u_t^2 A_p C_D = m_p g \quad (4.1)$$

where

$$F_D = \frac{1}{2} \rho_f u_t^2 A_p \frac{24}{Re_p} = \frac{1}{2} \rho_f u_t^2 A_p \frac{24 \mu_f}{\rho_f d_p u_t} \quad (4.2)$$

$$\begin{aligned} u_t &= \frac{m_p g}{3 \mu_f \pi d_p} = \frac{\rho_p d_p^2 g}{18 \mu_f} \\ &= \frac{983 \times (100 \times 10^{-6})^2 \times 9.81}{18 \times 1.11 \times 10^{-5}} \\ &= 0.482644 \frac{m}{s} \end{aligned} \quad (4.3)$$

Numerical solution

A grid independency on this domain is done and the results are shown in Table 4.1. The cell size is divided two times from 20 mm to 5 mm and no difference in results is observed for the average terminal velocity of a few droplets. Figure 4.1 show the velocity of the falling droplets.

Table 4.1: Grid independency for the Terminal velocity of a 100 μm droplet

Cell size [mm]	Terminal velocity [m/s]
20	0.465035
10	0.465035
5	0.465035

An independency on the step length factor is also done. The step length factor is the number of integration intervals per cell. The more intervals used the more accurate the solution. Table 4.2 show the solutions for different step length factors. The first step length factor is 5 from where it is doubled and the velocity is then measured. The step length factor is then doubled again and compared again to the previous result.

Table 4.2: Step length factor independence

Step length factor	Velocity [m/s]
5	0.465035
10	0.465035
20	0.465035

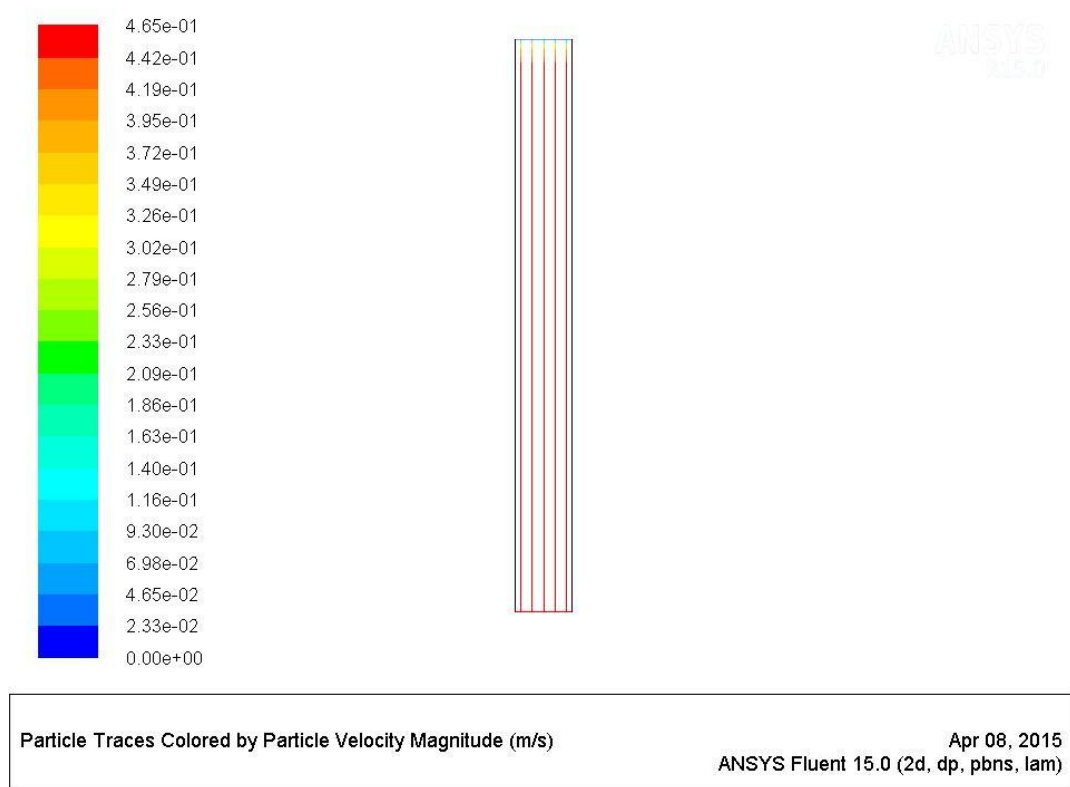


Figure 4.1: Velocity of 100 micron droplets falling under the force of gravity

It can be seen that there is no difference in results and any step length factor can be used. The velocity at which the droplets stop to accelerate is 0.465035 m/s and reaches this velocity after the droplet falls 0.30581 m. Figure 4.2 shows the velocity of the falling droplets and the data regarding the distance the droplets fall to reach the terminal velocity is shown in Appendix B.1. The terminal velocity of these size droplets is then calculated analytical and compared to the simulation result. The results of the analytical solution are different from the numerical solution with a small margin.

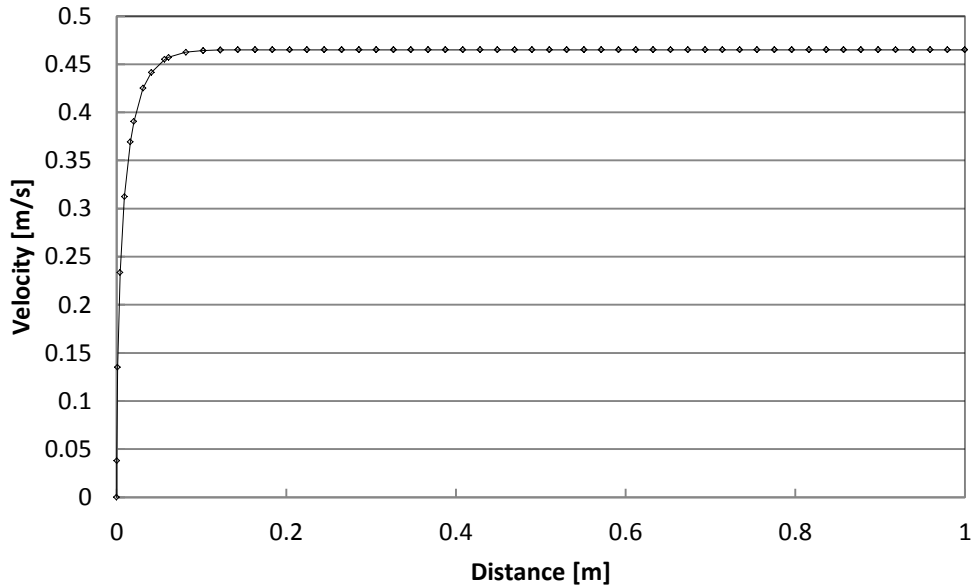


Figure 4.2: Average velocity of 100 micron droplets falling under the force of gravity

There is a 3.8 % difference in the analytical and numerical solution regarding the terminal velocity of a 100 μm droplet. If the pipe diameter is doubled to 0.2 m the same terminal velocity is reached.

4.2 Geometry, mesh and grid independence

The geometry of the duct and formulation of the flow problem is explained in this section from where the grid independence is discussed.

4.2.1 Geometry

The domain used for this study is shown and described in Figure 2.2. Only a certain part of the duct was used to simulate the flow problem to reduce cell count. Figure 4.3 shows the dimensions of the flow domain, which starts at five metres above the first bend below the LPT outlet and ends five metres above the second bend going to the ACCs, as shown in Appendix A.1. The bend at the LPT outlet and the vaned first bend would impose an influence on the flow pattern that

the effect of the inlet profile can be expected to be reduced when the flow reaches the second bend, which is the area of importance.

The end of the flow domain had to be of sufficient length whilst being as short as possible to reduce simulation time downstream of the second bend so that there would be no backflow through the outlet boundary. Figure 4.3 shows the geometry of the duct.

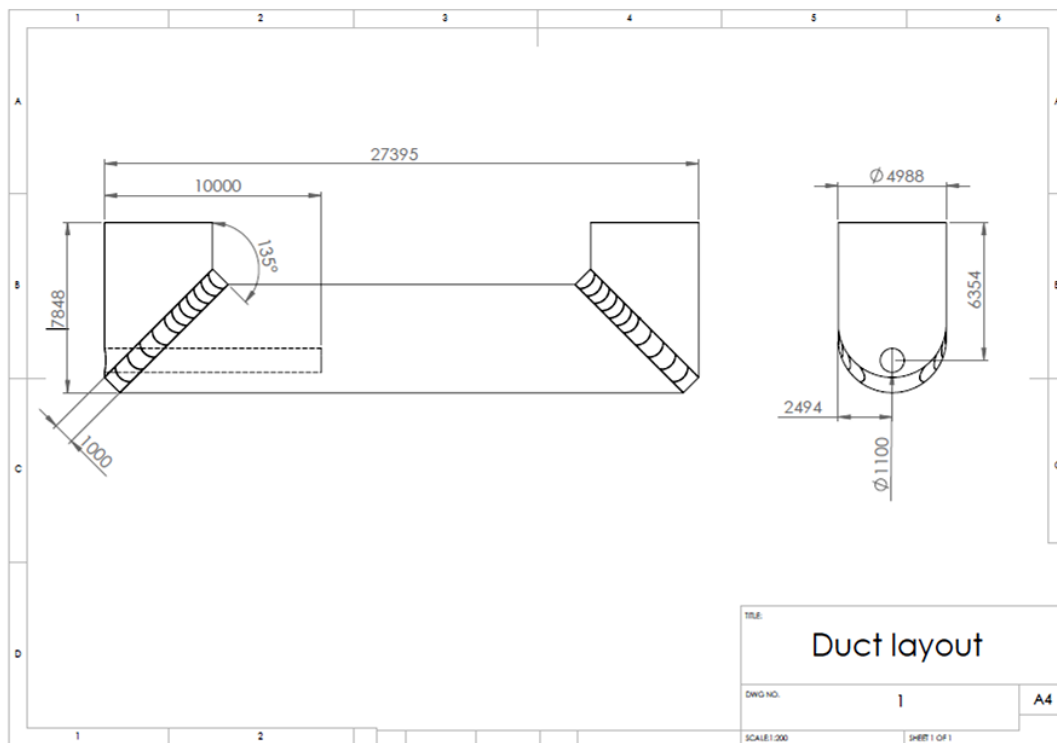


Figure 4.3: Layout and dimensions of the duct

4.2.2 Mesh

The flow domain grid is applied to the geometry of the CFD model in order to identify the discrete volumes or elements where the conservation laws must be applied (Tannehill, Anderson & Pletcher, 1997).

4.2.2.1 Mesh structure and topology

The fastest and easiest grid to use for a three dimensional rounded duct is an unstructured grid. In this arrangement, the grid imposes no implicit structure of

coordinate lines and the mesh can be easily concentrated in certain areas without wasting computer storage capacity. There are also no restrictions on the number of adjacent cells meeting along a line. This grid is also perfect for flow in or around geometrical features (Versteeg, 2007).

When setting up the grid for this application, setup time and computational expense must be taken into account. The geometry is relatively complex because of the angled vanes, so an unstructured tetrahedral grid will generate more quickly than structured or block-structured grids. This allows for saving time when several grid changes have to be made. Structured or block-structured grids carry the risk of overlapping geometry, mesh quality issues and a less efficient mesh distribution. This is because the tetrahedral mesh allows clustering of cells in selected regions of the flow domain. Hexahedral meshes permit a larger aspect ratio and less skewness, which provides more accuracy and less convergence time for simpler geometries. Polyhedral elements can be used in strategic places to reduce cell count, which quickens convergence time at the expense of a coarser mesh with less accuracy (ANSYS, 2012).

4.2.2.2 Computational domain

For this grid independence, the duct is divided symmetrically along the flow path of the steam to reduce cell count. Only the first half of the flow domain in Figure 4.3 is simulated because this part is considered to be the most complex, since the bypass is present in this part of the duct.

The tetrahedral cells in Figure 4.4 were converted into polyhedral cells to reduce cell count and to ease calculation activities. The cells were less skewed after the conversion, and the calculation activities were enhanced by these changes. Figure 4.4 shows the meshed first half of the duct with annotations indicating the boundary conditions and the bypass structure.

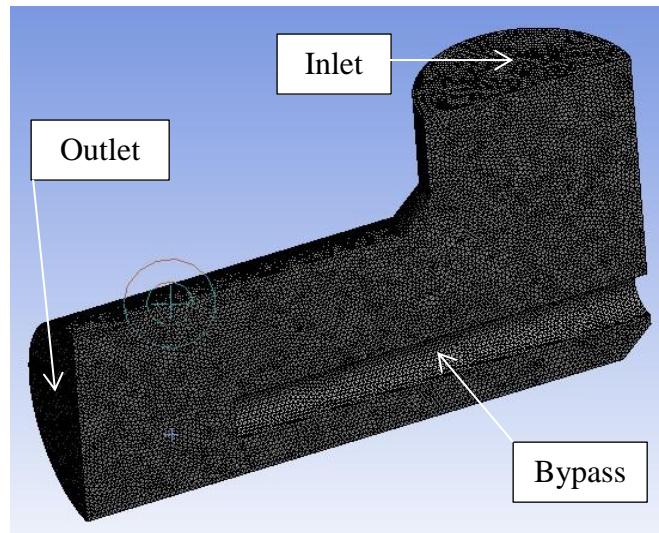


Figure 4.4: Meshed first half of the duct with tetrahedral cells used for grid dependency

4.2.2.3 Mesh parameters

Cell sizes are decreased from 0.2 m per cell to 0.075 m per cell, and the difference in pressure is examined. This cell size is then reduced till the change in pressure drop is less than 1 %. This margin is very small and the grid size would be sufficient for the rest of the simulations.

4.2.2.4 Properties of fluids

The properties of the vapour and the droplets are given in Table 4.3 and are calculated properties for 60 °C and 19.8 kPa operating conditions. The average velocity of the steam flowing at 204 kg/s in a 4.988 m diameter duct is used which calculates to 76 m/s.

Table 4.3: Properties of fluids

Parameters [units]	Symbol	Value
Vapour density [kg/m^3]	ρ_v	0.13
Vapour dynamic viscosity [kg/s.m]	μ_v	0.000011
Vapour inlet velocity [m/s]	U_v	76

4.2.2.5 Control parameters

Relaxation factors

A number of simulations were run simultaneously on a high-performance computer. For each simulation, there is a case, journal and submission file. To ensure that the simulations would run smoothly, without divergence in residuals, the momentum relaxation factor was changed from the default value of 0.7 to 0.1. The reason for this was that possible mesh quality issues could arise when the grid became very fine. Table 4.4 show these factors.

Table 4.4: Relaxation factors

Relaxation factors	Value
Pressure	0.3
Density	1
Momentum	0.1
Turbulent kinetic energy (k)	0.8
Specific dissipation rate (ω)	0.8
Turbulent viscosity	1

4.2.2.6 General information

The minimum orthogonal quality of the mesh is 0.27, which is sufficient for computation smoothness, the maximum aspect ratio of cells is 11.4, which is also sufficient for computation smoothness, the pressure-based solver is used, since the density is assumed to stay constant, gravity of 9.81 m/s^2 is enabled, which is only of significant importance when large droplets are injected, and the standard k - ω model with the second-order upwind discretisation scheme is selected.

4.2.3 Boundary conditions

The highlighted surfaces illustrate the boundaries explained.

4.2.3.1 Walls

The three boundaries of the flow domain to be set as walls are illustrated in Figure 4.5 (a) and (b), which are the wall of the duct, the vanes and the bypass. Because there was a liquid film on the edges of the walls, the roughness of the wall could be neglected.

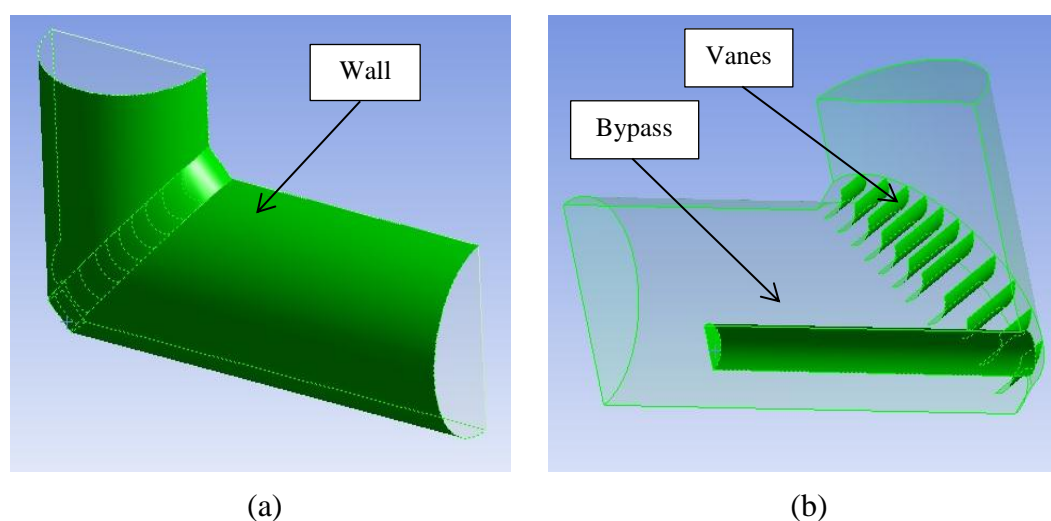


Figure 4.5: Here (a) shows the wall boundary of the outside edges of the flow domain, and (b) illustrates the vanes and bypass wall boundary condition.

4.2.3.2 Inlet and outlet

Both boundaries are given the same turbulence intensity and length scale. The values of the inlet and outlet boundary conditions are given in Figure 4.6 and Table 4.5. At the downstream side, after the wake at the trailing edge of the blades of a turbo machine, the turbulence intensity is estimated as 10 % (Ubaidi, Zunino & Cattanei, 1994). In a high-turbulence case, the turbulence intensity should vary between 5 % and 20 %.

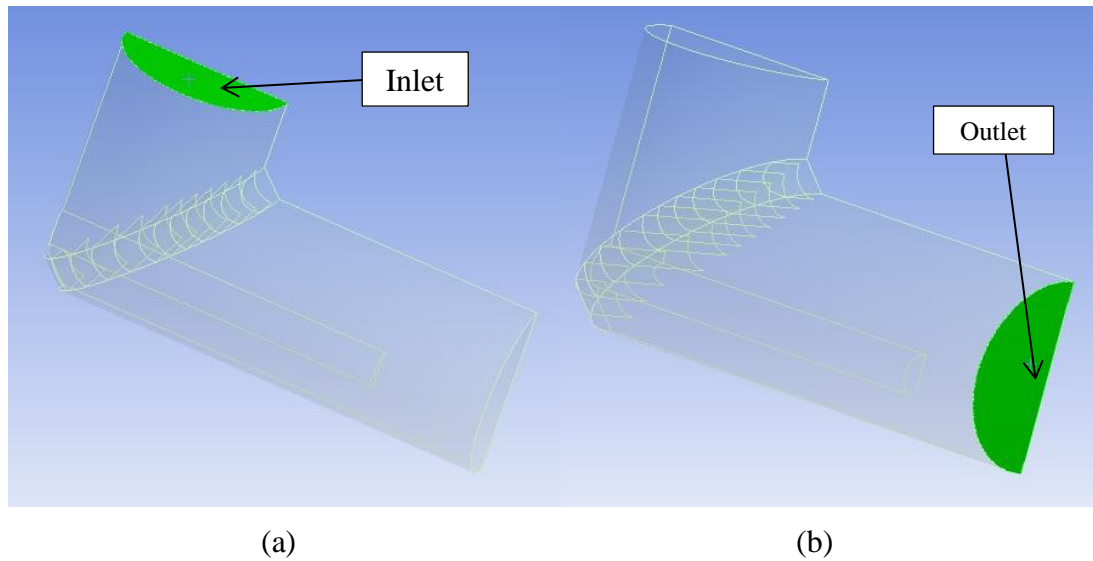


Figure 4.6: Inlet (a) and outlet (b) boundary conditions

The inlet pressure is calculated when a velocity inlet and a pressure outlet is specified.

Table 4.5: Inlet and outlet boundary conditions

Boundary	Value	Unit
Absolute inlet velocity	76	m/s
Inlet total pressure	0	kPa
Outlet total pressure	19.8	kPa
Turbulence intensity	10	%
Hydraulic diameter	4.988	m

4.2.3.3 Symmetry

For a symmetrical boundary, the velocity component normal to the boundary is zero and the gradient of all variables across the boundary is zero. Figure 4.7 shows this boundary condition.

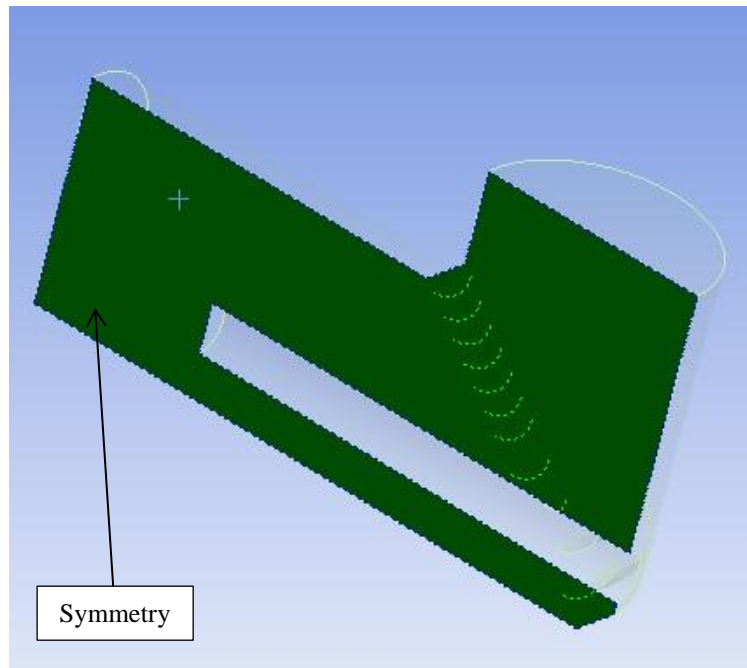


Figure 4.7: Symmetry boundary condition

4.2.4 Grid independence

The verification process is carried out to demonstrate the accuracy of the developer's conceptual description of the model and the solution to the model. This can be done by identifying and quantifying the errors in the model implementation and the solution. Iterative and grid convergence have to be evaluated to ensure accuracy of results.

4.2.4.1 Iterative convergence

Iterative convergence is reached when residuals drop under a prescribed value. Some design variables, such as pressure, need to be monitored to ensure that they reach a constant value.

4.2.4.2 Grid convergence

The smaller the size of the cells in a grid is, the more accurate the results will be. It has to be known whether the cell size used for the duct is sufficiently small to ensure accurate results. This can be determined by selecting an initial coarse grid

for the duct and solving pressure loss across the inlet and outlet boundaries of the duct. The grid then has to be refined, and the simulations have to be run again and solved for the same solution. The relative error is the fraction of change in result from the previous simulation and is calculated by the following equation.

The relative error ε is given by

$$\varepsilon = \frac{\Delta P_1 - \Delta P_2}{\Delta P_1} \quad (4.4)$$

(NPARC, 2012; Versteeg, 2007)

4.2.4.3 Results and discussion of grid dependence

The second-order upwind scheme was selected to simulate the grid independency. The results for the cell sizes are given in Table 4.6.

Table 4.6: Pressure drop for different cell sizes

Grid	Cell sizing (m)	P_{in} [Pa]	P_{out} [Pa]	ΔP [Pa]	Iterations
1	0.2	20 302	20 186	116	2 250
2	0.15	20 295	20 186	109	2 947
3	0.1	20 291	20 186	105	4 735
4	0.075	20 290	20 185	105	7 688

The relative error from grid 1 to grid 2 is

$$\varepsilon_{12} = \frac{116 - 109}{116} = 0.06 \quad (4.5)$$

and the relative error from grid 2 to grid 3 is

$$\varepsilon_{23} = \frac{109 - 105}{109} = 0.04 \quad (4.6)$$

Since there was no change in result from grid 3 to grid 4, the relative error should be zero.

4.2.4.4 Discretisation schemes

The first two orders of accuracy were tested to see which scheme was most suitable for this study. The first- and second-order upwind schemes were evaluated. Table 4.7 shows the results for both schemes selected to be evaluated.

Table 4.7: Evaluation of discretisation schemes

Scheme	ΔP	Iterations
First-order upwind	120	305
Second-order upwind	105	522

The second-order upwind scheme was selected for this study since it handles discontinuities in the flow field better than the first-order upwind scheme without consuming too much time.

4.3 Droplet size range

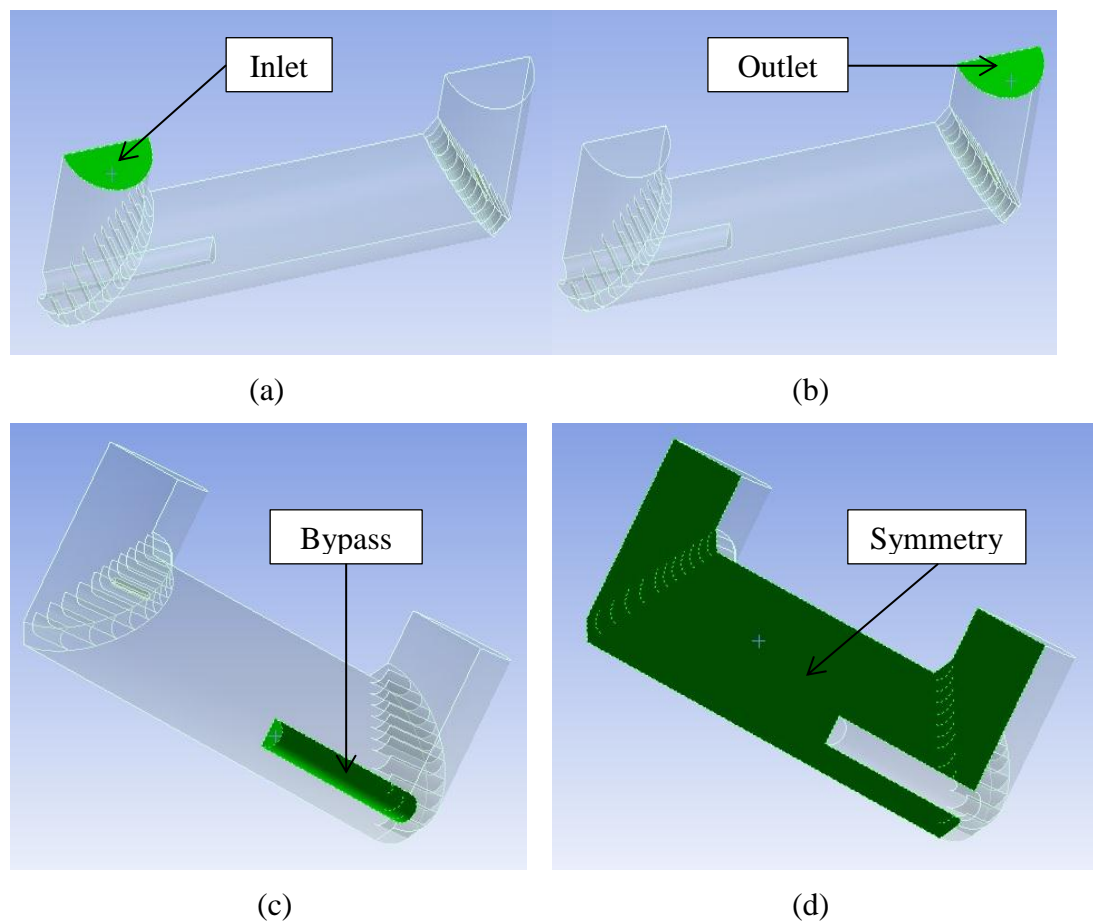
Since there is no information regarding the droplet size range, some assumptions should be made regarding the size range. Firstly the maximum droplet size is established by increasing the size of the injected droplets with every simulation. When the result regarding the amount of droplets that escape the domain and the amount that sticks to the wall film doesn't change, this size would be considered as the maximum droplet size in this range.

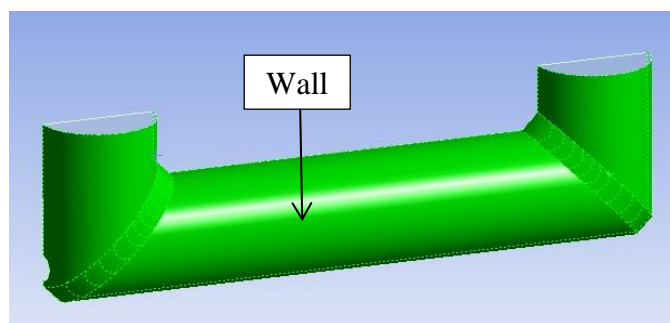
The same is done to establish the minimum droplet size for the droplet size range. The reason why the results will stop changing is due to the significance of the Stokes number where droplets will follow the fluid flow closely.

4.3.1 Computational domain

Boundary conditions for the full scale model are similar as for the grid independence study.

Figure 4.8 shows the boundary conditions of the full scale model. An inlet, outlet and symmetrical boundary condition are specified with wall boundary conditions on the bypass, vanes and wall of the duct. The highlighted areas illustrate these boundary conditions.





(e)

Figure 4.8: Here (a) and (b) are the inlet and outlet boundary conditions respectively, (c) represents the wall boundary condition at the bypass, (d) is the symmetrical boundary condition and (e) is the duct wall boundary condition

4.3.2 Results and discussion

The input parameters for the DPM are shown in Table 4.8. Since the relative velocity of droplets is very small in comparison with the velocity of steam for the majority of the droplets the same inlet velocity is given to the droplets.

Table 4.8: Properties of fluids and boundary conditions

Parameters (units)	Symbol	Value
Vapour density (kg/m^3)	ρ_v	0.13
Vapour dynamic viscosity (kg/s.m)	μ_v	0.000011
Vapour inlet velocity (m/s)	u_v	76
Droplet inlet velocity (m/s)	u_d	76
Droplet density (kg/m^3)	ρ_d	983
Droplet dynamic viscosity (kg/s.m)	μ_d	0.000463
Droplet mass flow rate (kg/s)	\dot{m}_d	5.1

The results regarding the maximum size range of the droplets are shown in Table 4.9. The droplet size was increased from a 100 μm till there is a small difference in results. The droplets that escaped the flow domain through the outlet surface

and that is absorbed (entrained) by the liquid film on the walls of the duct are measured.

Table 4.9: The maximum droplet size for the size range

Size [μm]	Tracked	Escaped	Absorbed
1000	1 110	29	1 081
600	1 110	30	1 080
500	1 110	31	1 079
400	1 110	34	1 076
300	1 110	43	1 067

There is no significant change in results for droplets larger than 500 μm . This is the maximum droplet size to do the rest of the simulations on.

The injection velocity of the 500 μm droplet is then simulated at 56 m/s and 66 m/s to see what influence the inlet velocity has on the results. Table 4.10 shows these results and it can be seen that there is no difference.

Table 4.10: The 500 micron droplet's flow behaviour when the inlet velocity is varied

Inlet velocity [m/s]	Tracked	Escaped	Absorbed
76	1 110	31	1 079
66	1 110	31	1 079
56	1 110	31	1 079

The minimum size for the droplet size range is determined in the same way. The size of the droplets is decreased till there is no change in results observed. Table 4.11 shows the results for the minimum size range.

Table 4.11: The minimum droplet size for the size range

Size [μm]	Tracked	Escaped	Absorbed
0.1	1 110	1 057	53
1	1 110	1 057	53
5	1 110	1 053	57
10	1 110	1 015	95

There is a slight change in results when droplets were decreased from 5 μm to 1 μm and from there the results don't change. The minimum size range is therefore 1 μm . It can be seen that the larger the droplet the more droplets get entrained by the film. This is due to the fact that more large droplets come in contact with walls in the duct due to their large inertia.

4.4 Submodels

Three submodels were investigated, namely the drag law-, the external force- and the wall film model. The results for each submodel will be discussed in its own section.

4.4.1 Drag law

In the literature study, it was shown that the Spherical drag law had to be used for this study since the droplets have Weber numbers below 0.14. It is quite a distance from 12 which is the critical Weber number for all droplets and so significant deformation of droplets is not expected. The maximum droplet size is used for this simulation since this size will be influenced mostly by the external aerodynamic forces.

Results of the SDL model and DDL models

The results of these models are given in Table 4.12. Together with the DDL a critical weber number of 12 are used to enable the stochastic secondary droplet breakup model. Shed refers to number of new droplets formed if breakup occurs.

Table 4.12: Effect of the SDL and DDL on the accretion rate on the vanes and droplet breakup

Droplet size [μm]	Drag law	Accretion rate [$\text{kg}/\text{m}^2\text{-s}$]	Deviation	Shed
1	SDL	6.53E-24	0.00 %	0
	DDL	6.53E-24		0
100	SDL	1.01E-22	1.32 %	0
	DDL	1.02E-22		0
200	SDL	1.01E-22	3.49 %	0
	DDL	9.84E-23		0
500	SDL	9.63E-23	5.88 %	0
	DDL	9.09E-23		0

There is no droplet breakup as calculated in section 3.4 but some deformation in droplet shape when it comes to large droplets. There is some deviation in accretion results on the vanes and the deviation increases as the droplet size increases which proves that the larger the droplet the greater the effect the aerodynamic forces has on the droplets. Even though the deviation is still small for a 500 μm droplet the DDL is still used for the rest of the study.

4.4.2 External forces

There are three external forces working on the droplets. Gravitation, the Saffman's force and the Magnus force. According to section 3.6, no significant Magnus or Saffman's forces can be expected when particles are following the fluid flow closely which is confirmed by the calculations that the larger the droplet the bigger all three forces will be on the droplet. Three droplet sizes in the established droplet size range are injected into the flow domain to see what the accretion rate on the vanes in the bends will be. The accretion rate on the vanes is of importance since this parameter is used to investigate which vane in the second bend can extract most of the liquid. The Saffman's force and gravity force is

disabled and enabled in Table 4.13 independently and the effect of these forces on the accretion rate on the vanes in both bends is shown.

Table 4.13: Accretion rate of different size droplets on the vanes

Droplet size [μm]	Force enabled	Accretion rate for the Saffman's force [$\text{kg}/\text{m}^2\text{-s}$]	Deviation	Accretion rate for the gravity force [$\text{kg}/\text{m}^2\text{-s}$]	Deviation
1	No	6.53E-24	0.00%	6.53E-24	0.00%
	Yes	6.53E-24		6.53E-24	
200	No	1.01E-22	0.38%	1.01E-22	0.75%
	Yes	1.01E-22		1.0184E-22	
500	No	9.63E-23	0.43%	9.47367E-23	1.59%
	Yes	9.59E-23		9.63E-23	

There is a small difference in results when the gravity force is disabled or enabled and does not make a significant difference in accretion rate results on the vanes. The Saffman's force's deviation from the enabled to the disabled force is also very small and this force won't make a significant difference in accretion rate results on the vanes and can be neglected for this droplet size range. This confirms that the gravity force has a greater influence on the droplets than the Saffman's force which correlates to the calculations done in section 3.6 so it is a good assumption that the Magnus force can also be neglected. It is also proved that the greater the droplet size the greater effect these forces have on the trajectory of the droplet.

4.4.3 Wall film model

It has to be confirmed what influence the thickness of the water film has on the entrainment of the droplets and to prove the theory that the thickness of the film would have no difference on the entrainment of droplets from one thickness to another, as described in Section 3.7. The film is solved by the momentum equation with particles, which could stick to or rebound from the film with gravity

and surface shear forces acting as forces. The film is assumed to have the same properties as the droplets due to both is exposed to the same duct conditions. In this submodel, a clean steam flow simulation was converged for different film thicknesses. Five random droplet sizes are used in the range. A droplet size of 500 μm is used for this submodel since it was proved that the amount of droplets that stick to the film for the size range is the most and the effect can be measured easier.

The results are given in Table 4.14, and it is apparent that the thickness does not make any difference in water entrainment results. Three films with thickness of 1 μm , 200 μm and 500 μm is simulated. At all film heights 1 079 droplets were entrained by the liquid film and 31 droplets escaped the flow domain, which confirmed the calculations described in Section 3.7. This proves that any height can be used for this study since the results is almost the same for all film heights.

Table 4.14: Behaviour of droplets for different size film heights

Film height [μm]	Tracked	Escaped	Absorbed
1	1 110	31	1 079
200	1 110	31	1 079
500	1 110	31	1 079

4.5 Separator design

An aerodynamic separator needs to be designed to extract liquid at the smallest pressure loss expense possible. Shapes identified in section 3.8 are evaluated. The vane which can extract most of the liquid also is identified.

4.5.1 Shapes

It can be seen from section 3.8 that the airfoil will cause the lowest pressure loss and a flat plate has the highest pressure loss for the same flow rate and frontal area

when it comes to a low speed wind tunnel. This statement is evaluated in this section for turbulent flow. In Figure 4.9 the velocity profile around vane five is shown where it can be seen that the vectors are almost directing parallel with the vane's downstream end. When the design of the separator is simulated it is assumed that the flow is in parallel with the shape of the object.

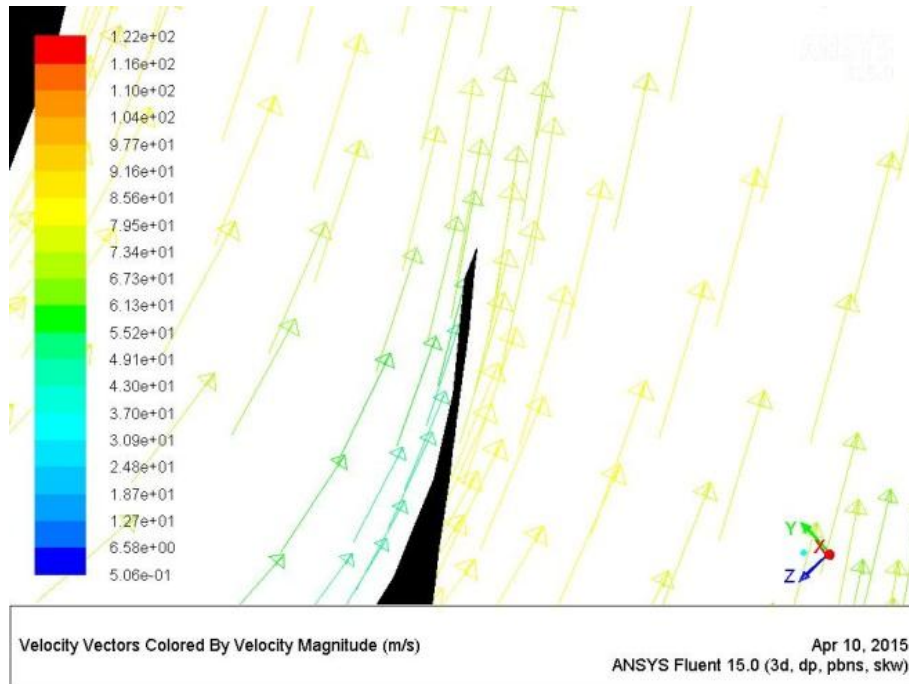


Figure 4.9: Velocity vectors passing the downstream end of vane five

The same dimensions as used in section 4.1 is used to do the grid independence for the two dimensional domain to evaluate the different shapes. A dimensional analysis is done to correlate the same conditions of this pipe to the conditions present on the power station. The Reynolds number must be the same for both cases.

$$Re = \left(\frac{\rho U D}{\mu} \right)_{power\ station} = \left(\frac{\rho U D}{\mu} \right)_{model} \quad (4.7)$$

Since the density and dynamic viscosity is constant, equation 4.4 simplifies to

$$(4.988 \times 76)_{power\ station} = (1 \times U)_{model} \quad (4.8)$$

$$U_{model} = 379 \frac{m}{s}$$

Table 4.15 shows the results of the grid independence for this two dimensional domain. The size of the cells, number of cells, pressure loss across the flow domain and deviation for the mesh refinement is shown.

Table 4.15: Grid independence for the two dimensional flow domain

Cell size [mm]	Number of cells	Pressure loss [Pa]	Deviation
100	1000	452.992	
50	3960	465.401	2.76 %
25	15800	466.152	0.16 %

From Table 4.15 there is a 2.76 % deviation in pressure loss from 100 mm refined to 50 mm cell sizing and a 0.16 % deviation from 50 mm cell sizing refined to 25 mm cell sizing. For this model a cell sizing of 50 mm is used.

Figure 4.10 shows the pipe with an inserted airfoil in the middle of the flow domain. The frontal area for all shapes is the same as for a 50 mm diameter sphere and the front tip of the objects is 5 m from the inlet of the pipe. The same boundary conditions as in section 4.1 is used and the pressure loss across the flow domain is monitored for all shapes. The tail of the airfoil is 200 mm long.

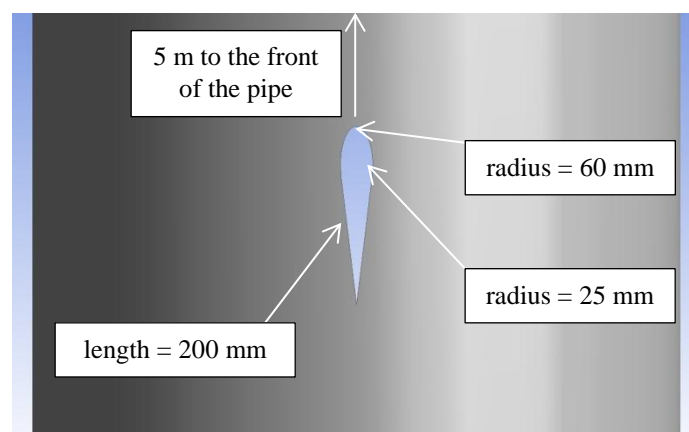


Figure 4.10: Airfoil geometry

In Table 4.16 the results for the pressure loss across the flow domain for all objects is shown.

Table 4.16: Pressure loss for five different shapes

Type	Pressure loss [Pa]
No object	465.401
Airfoil	675.77
Sphere	894.788
Bullet	934.967
Prism	1 171.395
Flat plate	1 509.756

From the results it is proven that the overall effect on pressure is the same for the turbulent flow in this case as for a low speed wind tunnel. The airfoil is the most effective shape followed by a sphere in terms of pressure loss and a flat plate is the worst. Figure 4.11-4.15 illustrates the velocity profile around each of these shapes.

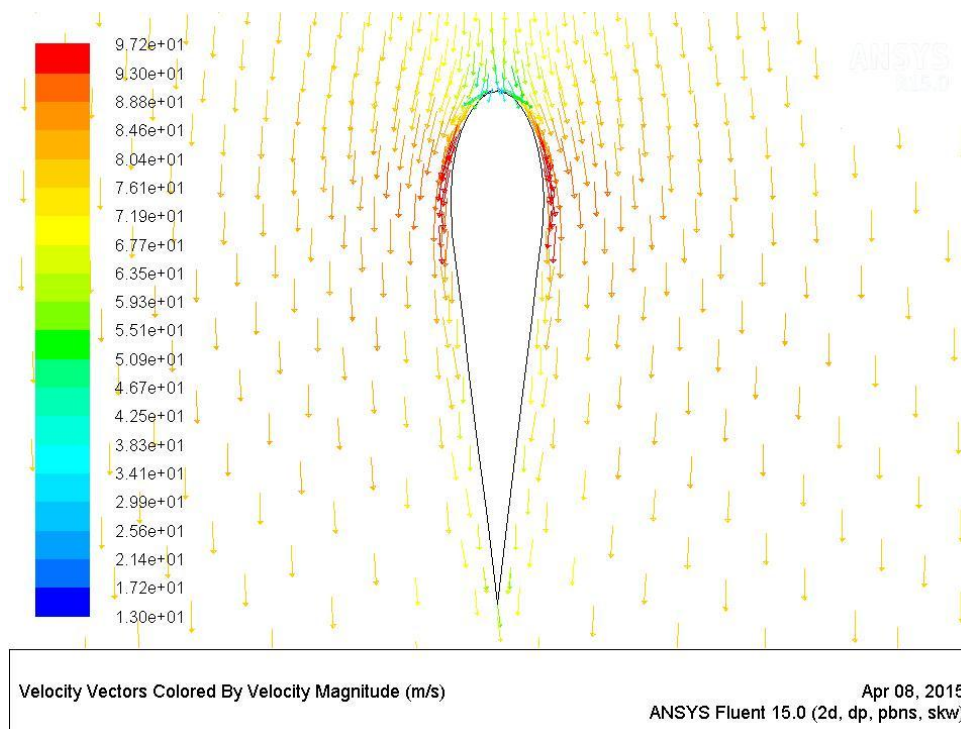


Figure 4.11: Velocity profile for the airfoil

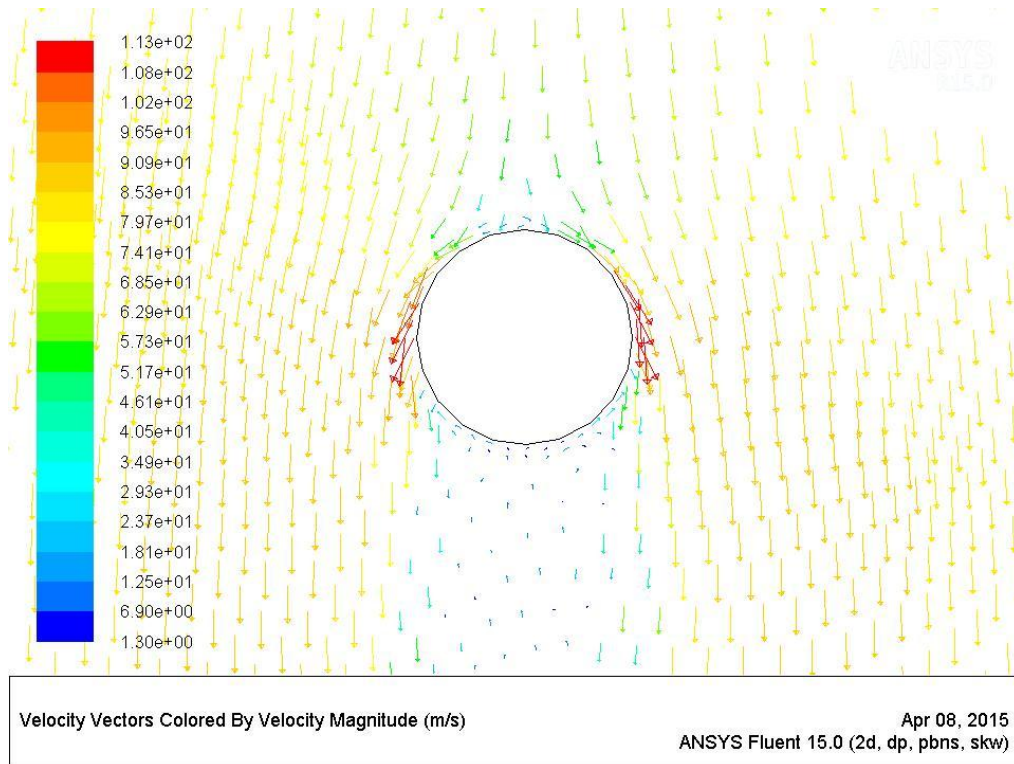


Figure 4.12: Velocity profile for the sphere

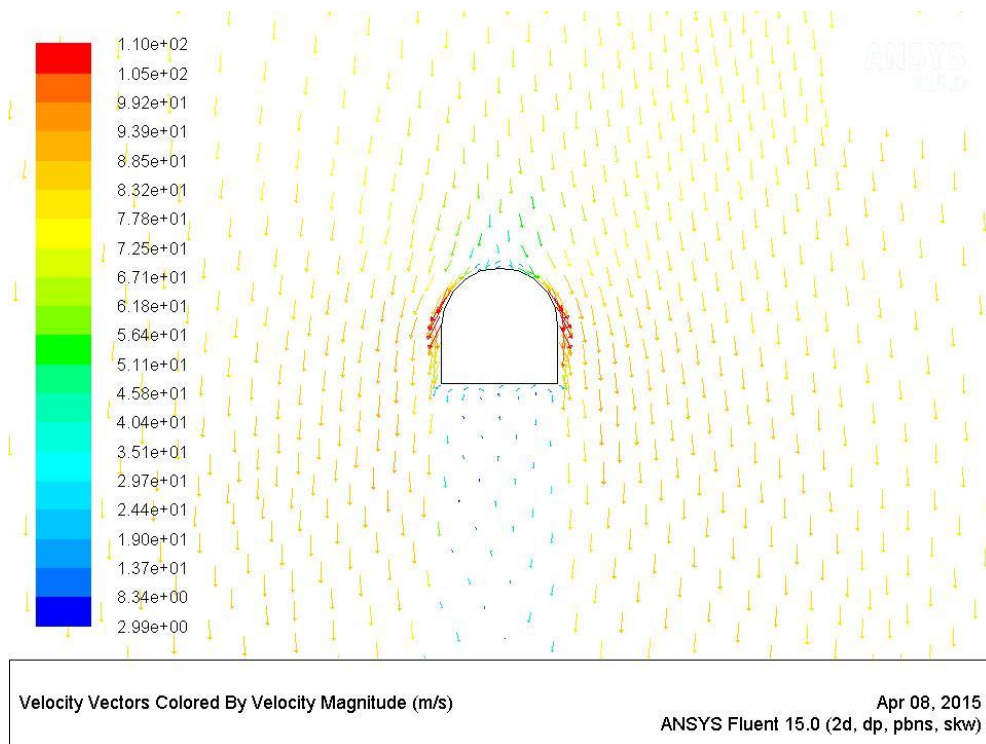


Figure 4.13: Velocity profile for the bullet

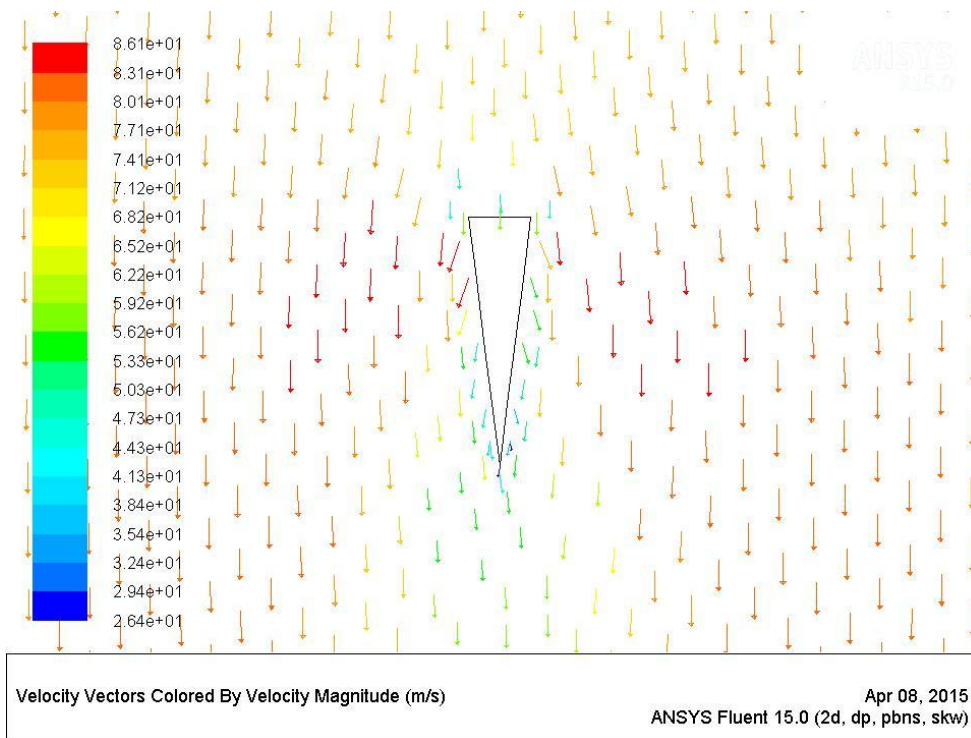


Figure 4.14: Velocity profile for the prism

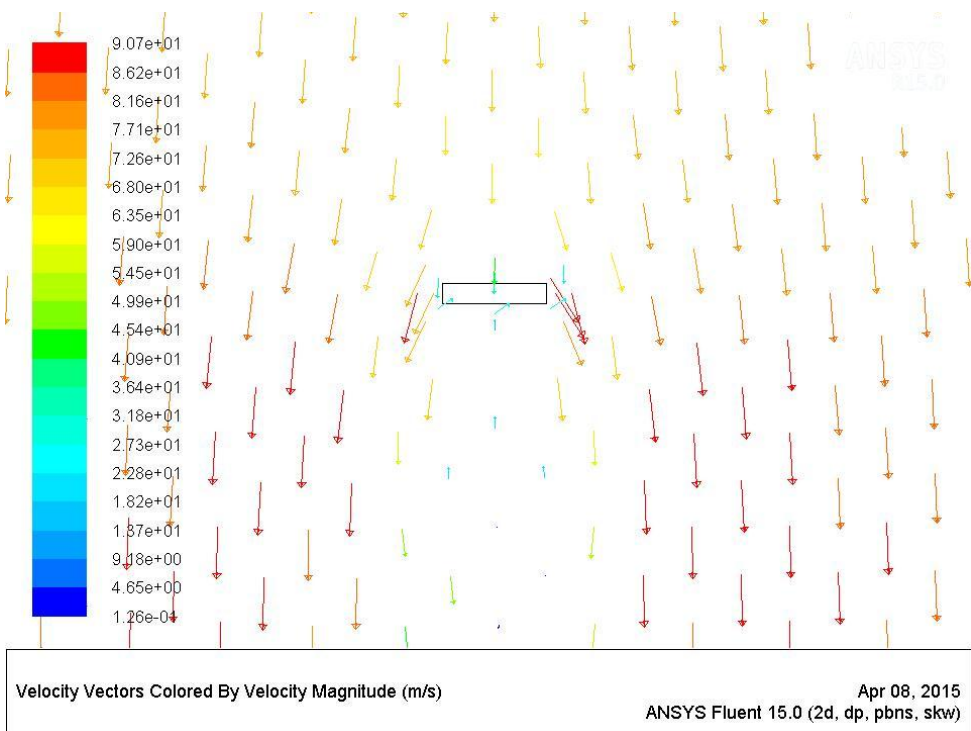


Figure 4.15: Velocity profile for the flat plate

The pressure loss increases as the velocity profile gets disturbed by the objects. It can be seen by looking at the above velocity profiles that the velocity at the downstream side of each object is decreased near the downstream side of the object. The airfoil which has the least pressure loss with minimum velocities of approximately 500 m/s at the downstream side while the flat plate have minimum velocities of approximately 300 m/s at the downstream side if the colour scheme of the velocity profiles is considered. It makes sense that the pressure is affected so much by the velocity profile since the dynamic pressure in a flow field is calculated by (Munson, 2006)

$$P_{dynamic} = \frac{\rho U^2}{2} \quad (4.9)$$

Now that the most aerodynamic shape for this flow domain is confirmed for turbulent flow too, it can be optimized to be more effective in terms of pressure loss.

4.5.2 Airfoil optimization

To optimize the airfoil shape there are different sensitivities to take in account to increase the aerodynamic effectiveness of the shape. Firstly the ratio of the two radiuses of the elliptical section must be optimized without the tail of the airfoil. From there a tail is added and the length of the tail is varied till the optimum point is reach in terms of pressure loss. Lastly the placement of the airfoil on the vane itself is evaluated to determine te optimum point for the airfoil to be placed on the vane.

4.5.2.1 Elliptical section of the airfoil

The tested airfoil's elliptical section had a ratio of 2.4 when 60 mm is divided into 25 mm. Different ratios are tested and the results is shown in Table 4.17. The small radius of the ellipse is 25 mm for all ratios. The ratio is taken from 2.4 till 5 and from there it is doubled till the pressure loss increases from the previous value. From there the optimum point is determined.

Table 4.17: Pressure loss for different radius ratios for the elliptical section of the airfoil.

Radius ratio	2.4	5	10	20	15	17	16	14	13
Pressure loss [Pa]	682.4	626.1	582.9	585.0	576.3	579.4	578.5	575.0	575.4

From the above results it can be seen that the most aerodynamic shape for the ellipse part of the object is 14. The velocity profile of an ellipse with a radius ratio of 14 is shown in Figure 4.16.

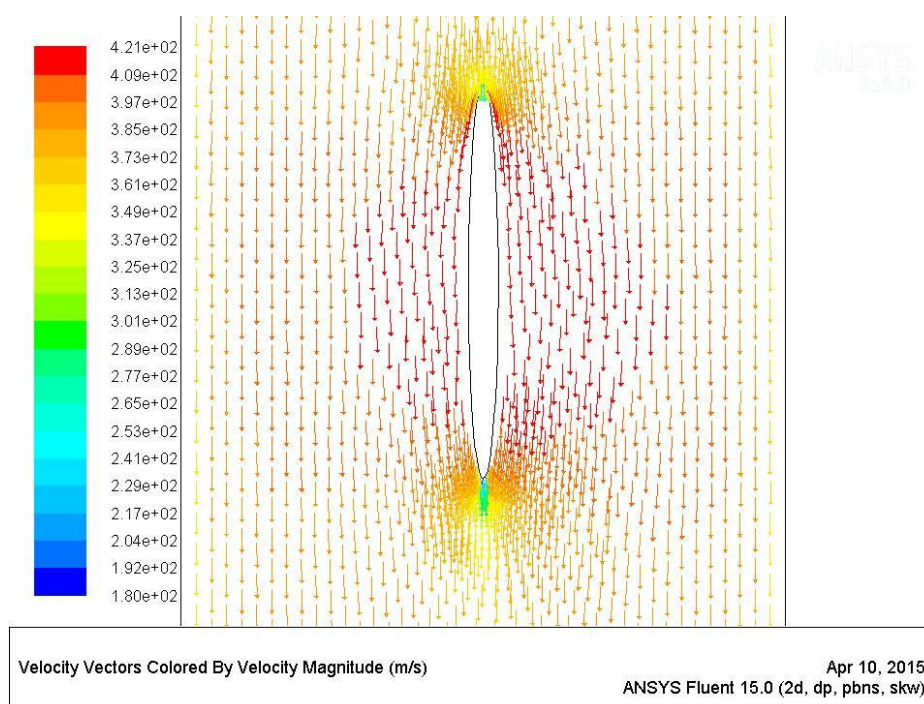


Figure 4.16: Velocity profile for the ellipse with a radius ratio of 14

4.5.2.2 Tail of the airfoil

From here a small 100 mm tail is added to optimize the elliptical section of the airfoil. This length is close to the elliptical shape of the separator. From there the tail is shortened to determine the optimum length of the airfoil’s tail. The tail of the airfoil is shown in Figure 4.17 where L12 is 90 mm.

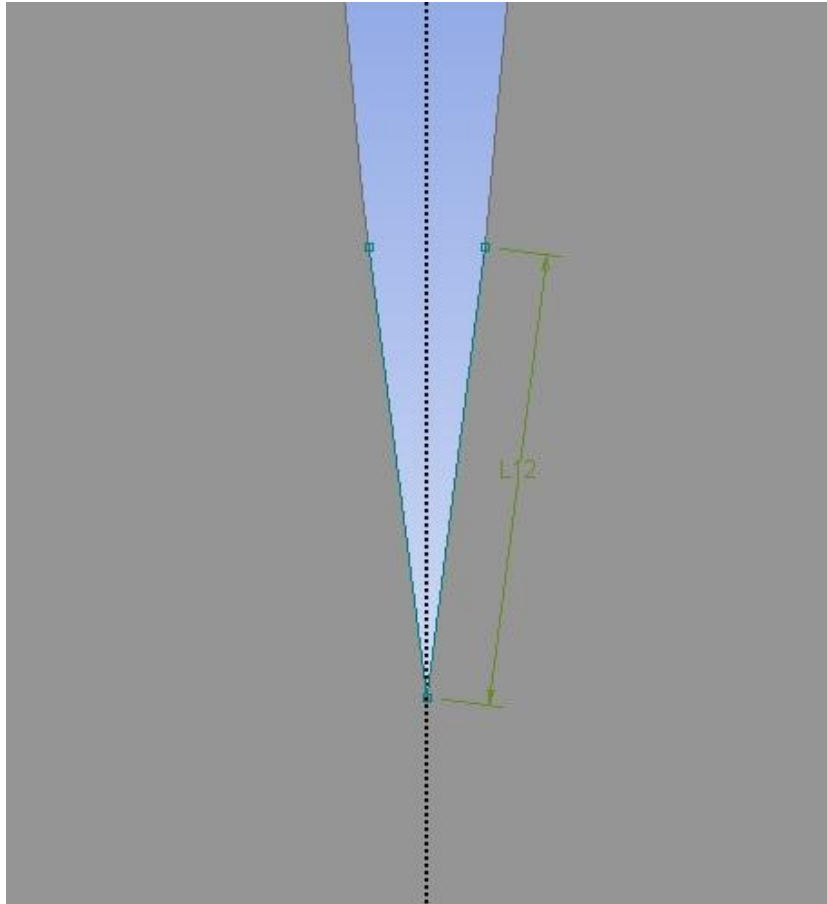


Figure 4.17: Tail extension of the airfoil with length 90 mm

Table 4.18 shows the results of the different tail lengths in terms of pressure loss across the flow domain. The optimum tail length for the airfoil is 90 mm.

Table 4.18: Effect of length of the tail extension in terms of pressure loss.

Tail length [mm]	No tail	100	50	95	90	80	85	91	81
Pressure loss [Pa]	575.0	574.8	579.8	573.6	572.1	575.1	575.5	573.5	572.4

In Figure 4.18 the velocity profile for the optimum airfoil is shown. There are fewer disturbances at the downstream side of the airfoil than the ellipse alone.

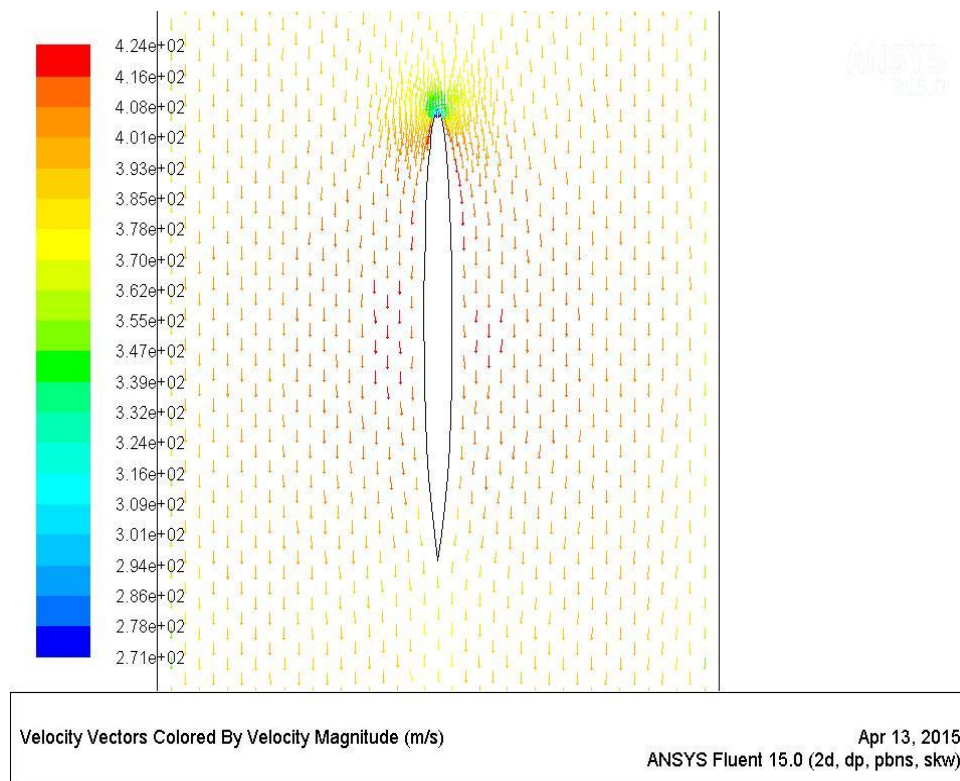


Figure 4.18: Velocity profile of the most aerodynamic airfoil

4.5.3 Liquid extraction on each vane

To know on which vane most of the liquid can be extracted it should be known which vane receives most of the droplets in terms of mass flow rate. It can be expected that water droplets that come in contact with a vane will stick to the liquid film on the vane or follow the fluid path along the surface of the vane which acts as a guide for the flow direction of the steam. The droplets that come in contact with the vanes can be expected to be the liquid that can be extracted by the separator. Since the face areas of the vanes are different, the amount of liquid that can be extracted for a certain face area of the vane should be evaluated. A representation of the amount of liquid that collides with the vane surface is to analyse the accretion rate on each vane caused by the water droplets. The accretion rate of droplets on a surface is the total collected mass flow rate per surface area and is represented by the following equation (ANSYS, 2012).

$$\dot{R} = \sum_{p=1}^{N_{particles}} \frac{\dot{m}_p}{A_{face}} \quad (4.10)$$

Different droplet sizes are injected from the inlet surface of the flow domain at a mass flow rate of 5.1 kg/s. Each size simulated on its own. The accretion rate on each vane for each size is measured to see which vanes tend to extract most of the liquid that can be extracted. The vanes are numbered from top to bottom of the duct as shown in Figure 4.19.

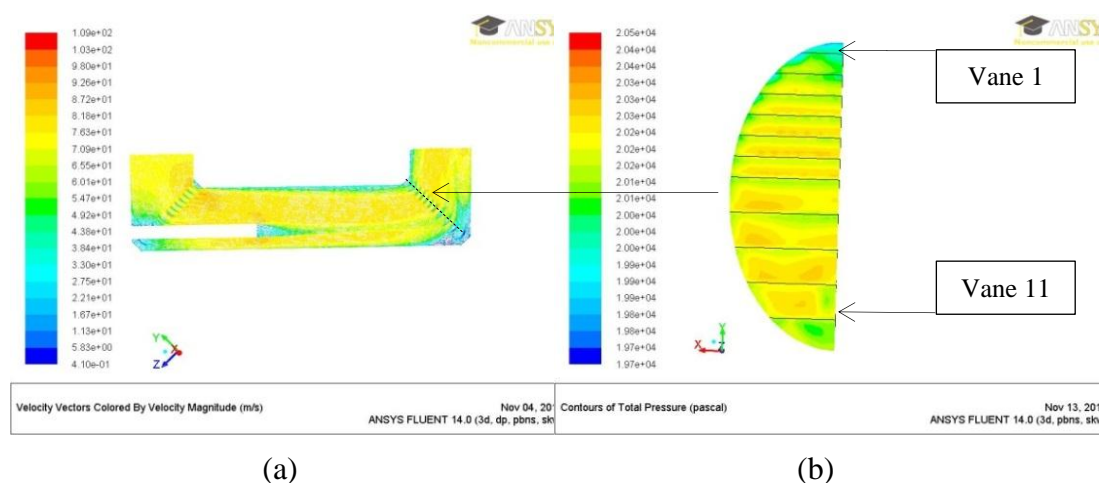


Figure 4.19: Here (a) is the velocity profile at the symmetric boundary of the duct and (b) is the pressure profile at the cross section illustrated in (a).

From Figure 4.19 it is clear that the highest steam velocities are between vane 2 and 11. The velocity profile also corresponds to the pressure profile if the colour scheme is considered.

Table 4.19 shows the results of the accretion rate of the different size droplets. These values can be converted to mass flow rate to see which vane extracts most of the liquid, irrespective of its collective surface area. The area of each vane shown in Table 4.20 is then multiplied by the accretion rate as indicated in Equation 4.13, to give the mass flow rate on each vane in as shown in Table 4.21.

Table 4.19: The accretion rate of the droplets in $\text{kg/m}^2\text{-s}$ that collides with the turning vanes.

Droplet size [μm]	1	10	20	50	100	200	500
Vane 1	0.0000	0.0000	0.0000	0.0000	0.0000	0.0090	0.0000
Vane 2	0.0000	0.0000	0.0000	0.0000	0.0000	0.0035	0.0115
Vane 3	0.0000	0.0000	0.0000	0.0026	0.0000	0.0080	0.0089
Vane 4	0.0019	0.0024	0.0000	0.0027	0.0000	0.0046	0.0026
Vane 5	0.0026	0.0000	0.0027	0.0048	0.0023	0.0153	0.0053
Vane 6	0.0014	0.0045	0.0043	0.0063	0.0000	0.0251	0.0010
Vane 7	0.0076	0.0083	0.0048	0.0019	0.0017	0.0287	0.0340
Vane 8	0.0000	0.0093	0.0033	0.0047	0.0000	0.0240	0.0219
Vane 9	0.0060	0.0026	0.0033	0.0102	0.0000	0.0164	0.0000
Vane 10	0.0021	0.0000	0.0086	0.0208	0.0127	0.0151	0.0050
Vane 11	0.0039	0.0000	0.0000	0.0000	0.0000	0.0000	0.0000

Table 4.20 shows the area of each vane.

Table 4.20: Area of each vane

	Area [m^2]
Vane 1	1.263545
Vane 2	1.788406
Vane 3	2.128410
Vane 4	2.365119
Vane 5	2.527829
Vane 6	2.630339
Vane 7	2.679580
Vane 8	2.649901
Vane 9	2.474132
Vane 10	2.116103
Vane 11	1.445459

Table 4.21: Capture rate of different sizes of droplets colliding with the turning vanes

Droplet size [μm]	1	10	20	50	100	200	500
Vane 1	0	0	0	0	0	0.0114	0
Vane 2	0	0	0	0	0	0.0063	0.0206
Vane 3	0	0	0	0.0055	0	0.0170	0.0189
Vane 4	0.0045	0.0057	0	0.0064	0	0.0109	0.0062
Vane 5	0.0066	0	0.0068	0.0121	0.0058	0.0387	0.0134
Vane 6	0.0037	0.0118	0.0113	0.0166	0	0.0660	0.0026
Vane 7	0.0204	0.0222	0.0127	0.0051	0.0046	0.0769	0.0911
Vane 8	0	0.0246	0.0087	0.0125	0	0.0636	0.0580
Vane 9	0.0148	0.0064	0.0082	0.0252	0	0.0406	0
Vane 10	0.0044	0	0.0182	0.0440	0.0269	0.0320	0.0106
Vane 11	0.0056	0	0	0	0	0	0

The results are randomly distributed and no vane can be definitely being selected to extract most of the liquid. Although the results are random it can be seen that vane seven receives droplets for all the droplet sizes and the larger droplets tend to move more towards the bottom vanes. This is due to the greater effect of gravity on the droplet and larger Stokes numbers. The 100 μm droplets have strange behaviour but yet no definite pattern can be determined. It can be safe to say that vane seven is the best vane to extract liquid in terms of mass flow rate. Vane one and vane eleven seem to receive very few droplets in terms of mass flow rate. In general it seems like vanes five to ten is good locations for separators.

4.5.4 Placement of the separator on the vane

The placement of the separator on the vane itself is also optimised. The separator must be as small as possible to decrease pressure loss through the flow domain.

The short radius of the separator is 7 mm so that 10 mm is behind the vane and the other 4 mm above the vane for liquid extraction. This is big enough to extract a liquid film of 4 000 μm . The long radius of the separator is shortened to 196 mm to result in a radius ratio of 14 which is determined as the most effective ratio for this type of flow.

Firstly the separator is placed with the middle of the elliptical section right onto the downstream end of the vane. From there the separator is moved forward on the vane each simulation to see if this has a beneficial effect on the pressure loss in the flow domain. Figure 4.20 shows the placement of the separator when the middle of the elliptical section is placed on the downstream end of the vane. The front of the separator is the same distance from the inlet of the flow domain as previously simulated and the vane is 10 mm thick with a length of 0.5 m.

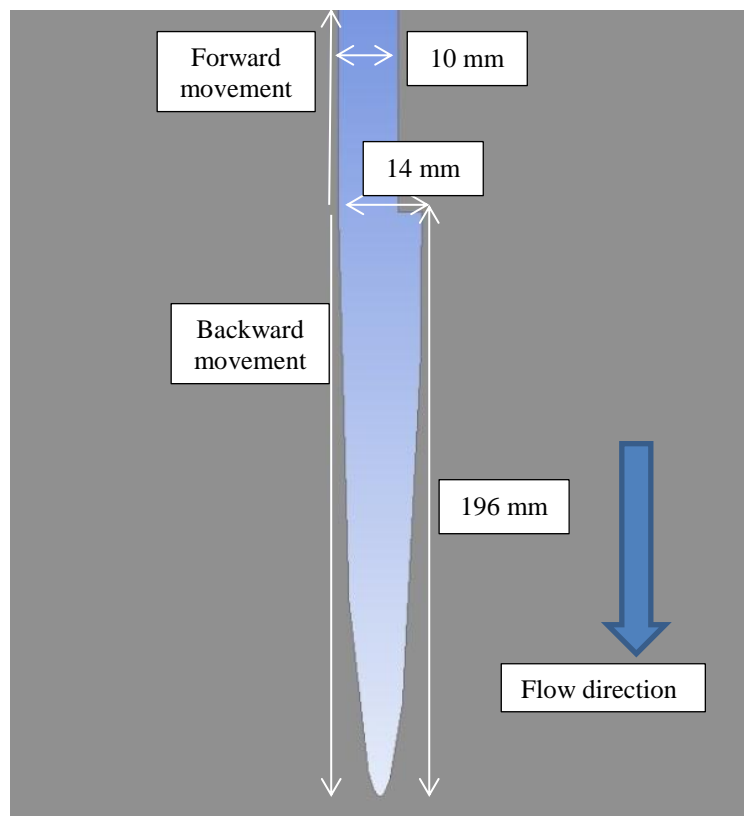


Figure 4.20: Separator placement on the vane

The separator is then moved forward on the vane by 10 mm and then 25 mm to see if the effect on pressure loss, followed by repeating the process for backward movement on the vane. In Table 4.22 the pressure loss for each placement is shown. It can be seen that the centred placement of the separator is the most aerodynamic.

Table 4.22: Effect of pressure when the separator is moved on the vane

Pressure [Pa]	No separator	Middle	10 mm	25 mm
Forward	523.75	506.92	512.68	514.17
Backwards	523.75	506.92	517.80	520.76

CHAPTER 5

CONCLUSION

When liquid extraction was done on the power station it was proved experimentally that liquid can be extracted using the guide vanes in the bend of the duct.

The numerical DPM could be validated with an analytical method within a 3.8 % margin. This confirms that the trajectories of the droplets are calculated correctly.

The droplet size range was determined when tests were done on the power station so a range of 1 μm to 500 μm was determined using a numerical approach. The size range is very important and is needed to determine what effect certain models and forces will have on the trajectories of the particles. This has to be done in situ, using sophisticated optical equipment, as liquid droplets coagulate once collected.

The terminal velocities of droplets were calculated below 12.08 m/s. The larger the droplet sizes the higher their terminal velocity. For the largest droplet in the range that would've been affected the most a velocity difference of 20 m/s didn't make any difference to the results. The terminal velocity is thus a good indication of what the relative velocity will be of the droplets in the duct.

Droplets larger than 350 μm were calculated to deviate from the flow field since the Stokes numbers of these droplets is more than one and the Stokes number increase as the droplet size increase. This could be seen during simulations where the droplet size range was determined. The larger the droplets the greater portion of the droplets get absorbed by the liquid film. It was shown analytically that the smaller droplet sticks to the liquid film more easily than the larger droplets because of their low impact energy, and they cannot escape the bonding energy of the film. The numerical results show that it is mostly the larger droplets that collide with the walls due to their higher inertia.

For the smaller droplets the significance of the Stokes numbers could be seen with Stokes numbers which were much smaller than one. There were no difference in results with droplet sizes of 1 μm and smaller. This is because they follow the fluid flow closely as specified in the literature study.

Droplets in this size range didn't break up in this type of flow as analytical calculated. The larger the droplet the easier they will break up. Although the Weber number of the large droplets was far from 12 and deformation of droplets wasn't expected, there was still a slight difference in the accretion rate of the droplets on the vanes when the DDL was used instead of the SDL. This confirms that the overall shape of the droplets is spherical with small deformation in shape when it comes to larger droplets. The larger the droplets the more the DDL results deviated from the SDL results. So if larger droplets than 500 μm is simulated the DDL should definitely be used.

Gravity has a small effect on the droplet trajectories because the droplet size range used were close or well below one. The Saffman's lift force affected the droplet trajectories less which corresponded well to the analytical solution so it is a good assumption that the Magnus force will have an even smaller effect on the droplet trajectories. The larger the droplet the greater effect the external had on the droplet trajectories.

An airfoil has the most aerodynamic shape of the objects tested. This statement is the same for turbulent flow in this case as for a low speed wind tunnel. A flat plate is the worst aerodynamic shape with a factor more than two in this case than an airfoil. This can be seen by looking at the velocity profiles at the downstream side of the the objects. The more disturbances were caused by the object in the velocity profile the greater the pressure drop across the domain was.

A radius ratio of 14 for the elliptical section of the airfoil was determined to be the most aerodynamic. The ellipse became more aerodynamic when the downstream side of the ellipse was extended with a tail section. For this application where the

vane is 10 mm thick, the radiuses of the airfoil should be 14 mm and 196 mm. The tail section must have a length of 90 mm and should be placed on the downstream side of the vane with the centre of the elliptical section on the downstream edge of the vane. This separator size is sufficient to extract liquid from a film which is 4 000 μ m thick.

Vane seven receives most of the liquid in the duct and also has the largest surface area of all vanes. Vane one and eleven extracted the least liquid and is also the two smallest vanes.

CHAPTER 6

RECOMMENDATIONS

A swirl at the outlet of the LPT might have an influence on droplets that hit the edges of the duct. Most of these droplets will be entrained by the liquid film on the wall of the duct since the droplets is thrown sideways by the plenum. The swirl will also have an influence on the flow pattern before the first bend where droplets can be entrained by the liquid film. After the first bend, the flow pattern will be influenced less by the swirl because of the guide vanes that force the flow in a certain direction. This was also the reason why the first bend was included in this study to reduce this uncertain swirling effect.

If liquid can be extracted from the edges of the duct during experimental work on the power plant, the distribution of the droplets can be predicted more accurately. If the size of droplets can be predicted that gets absorbed by the liquid film and the amount of liquid extracted from the duct on the power station, the more accurate the droplet size range can be predicted. The best will be if the droplet size distribution can be measured on the power station.

A structured mesh, in the regions of the duct where possible, would improve the convergence time and stability of the simulations.

The bottom vanes tended to receive more liquid than the top vanes. It is recommended to place a separator on vane five and vanes downward. An airfoil shaped separator with the dimensions identified in this thesis can be placed on vane seven to extract most of the liquid.

REFERENCES

- ANSYS (2012) *ANSYS Fluent 14.0 Theory Guide*. Canonsburg: ANSYS Inc.
- Dooley, R.B., Aspden, J.D., Howell, A.G. & Du Preez, F. (2009) *Assessing and controlling corrosion in air-cooled condensers*. *PowerPlant Chemistry*. 11 (5), 264.
- Eskom [2008] *Matimba Power Station* [Online]. Available: http://www.eskom.co.za/Whatweredoing/ElectricityGeneration/PowerStations/Pages/Matimba_Power_Station.aspx [2013, November 14].
- Kröger, D. (1998) *Air-cooled heat exchangers and cooling towers*. Stellenbosch: University of Stellenbosch.
- Liu, Y., You, L., Yang W. & Liu F. (1993) *On the size distribution of cloud droplets*. Jiaozhou, China: Institute of Environment Science.
- Manga, M. & Stone, H.A. (1994) *Low Reynolds number motion of bubbles, drops and rigid spheres through fluid-fluid interfaces*. Cambridge, Harvard University
- Mekis, A., Nöckel, J.U., Chen, G., Stone, A.D. & Chang, R.K. (1995) *Ray chaos and Q-spoiling in Lasing Droplets*. New Haven, Connecticut: Yale University.
- Munson, B.R., Young, B.F. & T.H. Okiishi (2006) *Fundamentals of fluid mechanics*. 5th ed. Hoboken: John Wiley and Sons.
- Northcott, K. (2011) *Internal degradation of ACCs – interim results and findings*. Lephalale: Eskom.
- NPARC Alliance. [2012] *Examining spatial (grid) convergence*. [Online]. Available: <http://www.grc.nasa.gov/WWW/wind/valid/tutorial/spatconv.html>. [2012, November 26].

NPARC Alliance. [2015] *Shape Effects on Drag*. [Online]. Available: <http://www.grc.nasa.gov/education/rocket/shaped.html>. [2015, January 11].

Ryley, D. (1967) *Condensation fogs in low-pressure steam turbines*. Liverpool: Department of Mechanical Engineering, University of Liverpool.

Tamini, S. (2012) *An Analysis of Developing Turbulent Flow*. Dubai, United Arab Emirates: ALGhurair University.

Tannehill, J.C., Anderson, D.A. & Pletcher, R.H. (1997) *Computational fluid mechanics and heat transfer*. 2nd ed. Washington: Taylor & Francis.

Tarnogrodzki, A. (1992) *Theoretical prediction of the critical weber number*. Warsaw, Poland: Technical University of Warsaw.

Ubaidi, M., Zunino, P. & Cattanei, A. (1994) *Relative flow and turbulence measurements*. Genova, Italy: University of Genova.

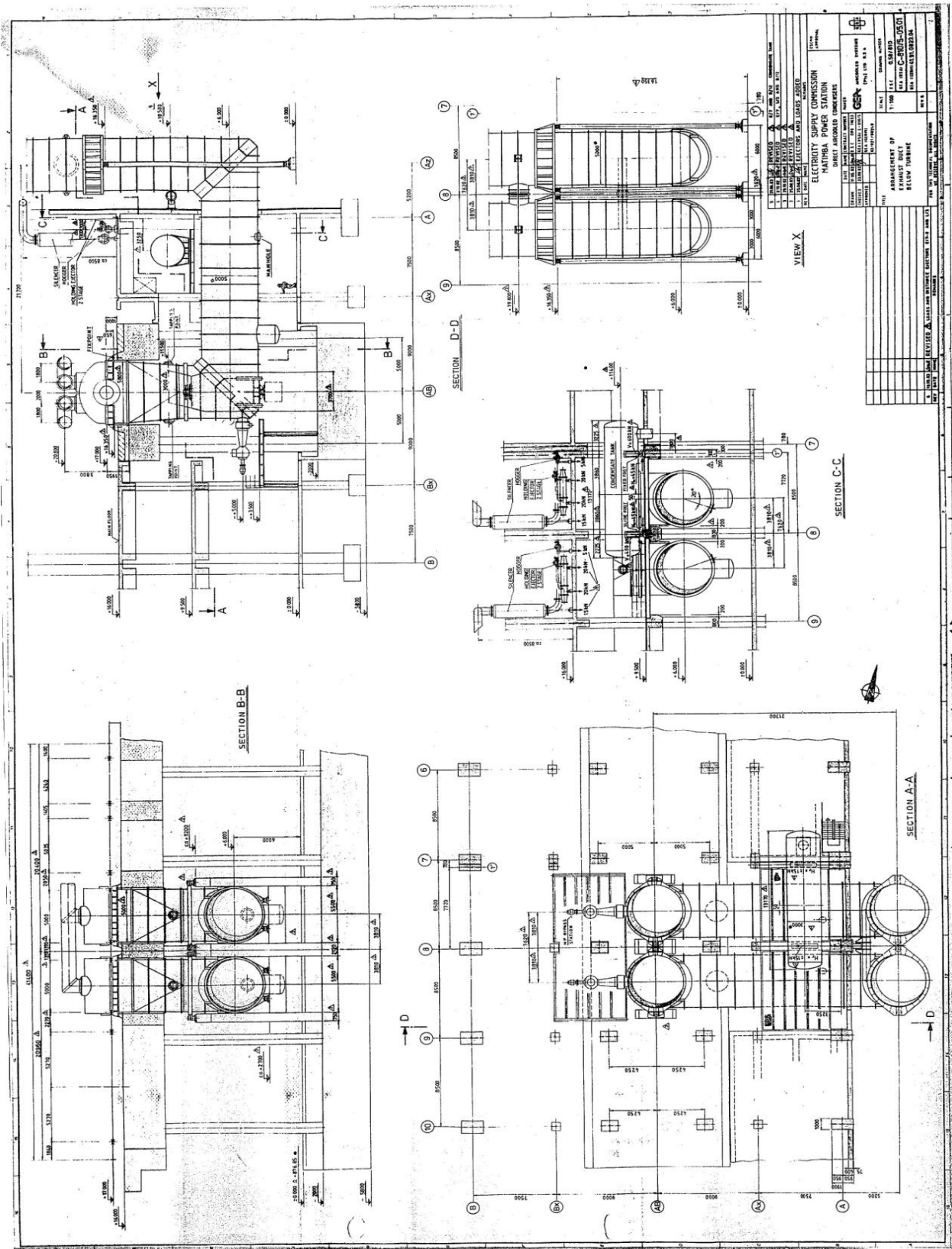
Van Thienen, P., Vreeburg, J.H.G. & Blokker, E.J.M. (2010) *Radial transport processes as a precursor to particle*. Nieuwegein, The Netherlands: ScienceDirect.

Versteeg, M. (2007) *An introduction to computational fluid dynamics: The finite volume method*. 2nd ed. Harlow: Pearson Education Limited.

APPENDIX A

DRAWINGS

A.1: Duct



APPENDIX B**DATA****B.1 Velocity of 100 μm droplets falling under the force of gravity**

Velocity (m/s)	Distance (m)	Velocity (m/s)	Distance (m)	Velocity (m/s)	Distance (m)
0	0	0.326538	0.465035	0.69367	0.465035
7.72E-05	0.0380389	0.346740	0.465035	0.693876	0.465035
0.00111866	0.135014	0.346946	0.465035	0.714078	0.465035
0.00411224	0.23372	0.367147	0.465035	0.714284	0.465035
0.00916481	0.312264	0.367353	0.465035	0.734486	0.465035
0.0161438	0.369345	0.387555	0.465035	0.734692	0.465035
0.0203266	0.390434	0.387761	0.465035	0.754893	0.465035
0.0311213	0.425075	0.407963	0.465035	0.7551	0.465035
0.0408154	0.441378	0.408169	0.465035	0.775301	0.465035
0.0564661	0.455016	0.428370	0.465035	0.775508	0.465035
0.0612373	0.457151	0.428576	0.465035	0.795709	0.465035
0.081646	0.462546	0.448778	0.465035	0.795916	0.465035
0.101939	0.464235	0.448984	0.465035	0.816116	0.465035
0.102055	0.464239	0.469186	0.465035	0.816323	0.465035
0.122267	0.464777	0.469392	0.465035	0.836524	0.465035
0.122462	0.464779	0.489594	0.465035	0.836731	0.465035
0.142666	0.464952	0.489799	0.465035	0.856932	0.465035
0.142869	0.464953	0.510001	0.465035	0.857139	0.465035
0.163071	0.464995	0.510207	0.465035	0.877339	0.465035
0.163277	0.464995	0.530409	0.465035	0.877546	0.465035
0.183477	0.465016	0.530615	0.465035	0.897747	0.465035
0.183684	0.465016	0.550817	0.465035	0.897954	0.465035
0.203885	0.465026	0.551023	0.465035	0.918166	0.465035

0.204092	0.465026	0.571224	0.465035	0.918381	0.465035
0.224293	0.46503	0.57143	0.465035	0.938591	0.465035
0.2245	0.46503	0.591632	0.465035	0.938794	0.465035
0.2447	0.465033	0.591838	0.465035	0.959034	0.465035
0.244907	0.465033	0.61204	0.465035	0.959202	0.465035
0.265109	0.465034	0.612246	0.465035	0.979447	0.465035
0.265315	0.465034	0.632447	0.465035	0.979638	0.465035
0.285517	0.465034	0.632653	0.465035	0.999823	0.465035
0.285723	0.465034	0.652855	0.465035	1	0.465035
0.305924	0.465035	0.653061	0.465035		
0.30613	0.465035	0.673263	0.465035		
0.326332	0.465035	0.673469	0.465035		